

日本磁気学会

ISSN 2432-0250

Journal of the Magnetics Society of Japan

Electronic Journal URL: <https://www.jstage.jst.go.jp/browse/msjmag>

**Vol.42 No.6 2018**

**Journal**

**Review: MSJ Awards 2017**

Magnetoelectric Control of Antiferromagnetic Domain of  $\text{Cr}_2\text{O}_3$  Thin Film Toward Spintronic Application

Y. Shiratsuchi, T. V. A. Nguyen and R. Nakatani ... 119

**Magnetic Recording**

Understanding Signal-to-Noise Ratio in Heat-Assisted Magnetic Recording

T. Kobayashi, Y. Nakatani, and Y. Fujiwara ... 127

---

# JOURNAL OF THE MAGNETICS SOCIETY OF JAPAN

Vol.42 No.6 2018

日本磁気学会

ISSN 2432-0250

HP: <http://www.magnetics.jp/> e-mail: [msj@bj.wakwak.com](mailto:msj@bj.wakwak.com)

Electronic Journal: <http://www.jstage.jst.go.jp/browse/msjmag>

# Journal of the Magnetism Society of Japan

## Vol. 42, No. 6

Electronic Journal URL: <https://www.jstage.jst.go.jp/browse/msjmag>

---

### CONTENTS

#### Review: MSJ Awards 2017

- Magnetoelectric Control of Antiferromagnetic Domain of Cr<sub>2</sub>O<sub>3</sub> Thin Film Toward Spintronic Application  
 ..... Y. Shiratsuchi, T. V. A. Nguyen and R. Nakatani 119

#### Magnetic Recording

- Understanding Signal-to-Noise Ratio in Heat-Assisted Magnetic Recording  
 ..... T. Kobayashi, Y. Nakatani, and Y. Fujiwara 127

---

### Board of Directors of The Magnetism Society of Japan

<b>President:</b>	K. Takanashi
<b>Vice Presidents:</b>	K. Nakagawa, S. Nakamura
<b>Directors, General Affairs:</b>	Y. Miyamoto, K. Niiduma
<b>Directors, Treasurer:</b>	K. Aoshima, K. Ishiyama
<b>Directors, Planning:</b>	Y. Saito, S. Nakagawa
<b>Directors, Editorial:</b>	K. Kobayashi, T. Ono
<b>Directors, Public Relations:</b>	H. Itoh, S. Greaves
<b>Directors, International Affairs:</b>	Y. Takemura, M. Nakano
<b>Auditors:</b>	Y. Suzuki, R. Nakatani

# Magnetoelectric control of antiferromagnetic domain of Cr<sub>2</sub>O<sub>3</sub> thin film toward spintronic application

Y. Shiratsuchi, T. V. A. Nguyen and R. Nakatani

Graduate School of Engineering, Osaka University, 2-1 Yamadaoka, Suita, Osaka 565-0871, Japan

Cr<sub>2</sub>O<sub>3</sub> is a magnetoelectric antiferromagnet, and its antiferromagnetic domain state is controllable by the simultaneous application of magnetic and electric fields. In the 2000s, that is, more than 50 years since the discovery of the magnetoelectric effect in Cr<sub>2</sub>O<sub>3</sub>, efforts were initiated to apply this effect to engineering applications. In this article, we review the recent progress of the magnetoelectric control of the antiferromagnetic domain state and the related phenomena of Cr<sub>2</sub>O<sub>3</sub>, in particular, in an all-thin film system, an essential step to the application.

**Key words:** magnetoelectric effect, antiferromagnetic domain, Cr<sub>2</sub>O<sub>3</sub>, thin film

## 1. Introduction

The interplay between magnetism and electricity has been known as the magnetoelectric (ME) effect, which is referred as the magnetization ( $M$ ) induction caused by an electric field ( $E$ ) and the electric polarization ( $P$ ) induction caused by a magnetic field ( $H$ ). The ME effect was predicted in the 19th century by Curie<sup>1</sup>. In 1920s, Perrier and Staring investigated this effect using Fe and Ni and proposed the existence of ME effect<sup>2,3</sup>. Later on, however, they corrected their experiment was wrong<sup>4</sup>. Meantime, Piccard suggested the impossibility of the effect on symmetry grounds<sup>5</sup>. After these research, Debye who first used the term of “magneto-electric” suggested that the ME effect was impossible<sup>6</sup> and Van Vleck described in his book the reason why the ME effect was impossible<sup>7</sup>. After 50 years later from the Curie’s proposal, Landau and Lifshitz dealt with this problem and showed that the ME effect should exist in magnetic crystal.<sup>8</sup> Based on the prediction by Landau and Lifshitz, Dzyaloshinskii predicted that Cr<sub>2</sub>O<sub>3</sub> was an actual candidate causing this effect<sup>9</sup>. Soon after the prediction, the  $H$ -induced polarization  $P^{(0)}$  and  $E$ -induced magnetization  $M^{(1)}$  were experimentally confirmed independently. After the discovery of the ME effect in Cr<sub>2</sub>O<sub>3</sub>, the research on this effect progressed to the field of “multiferroics”<sup>12</sup>. More details about the history of the ME effect can be found in textbook<sup>13</sup> and the progress of the ME effect after the early development can be found in previous review<sup>14</sup>.

As Cr<sub>2</sub>O<sub>3</sub> exhibits a linear ME effect, the removing field disperses the ferroic feature. This could partly be the reason why efforts to apply the ME effect of Cr<sub>2</sub>O<sub>3</sub> to engineering applications were not very active until the pioneering work by Borisov *et al.*<sup>15</sup>. Their idea is based on the fact that to complement the limitation of the linear ME effect, the ferromagnetic (FM) layer coupled with Cr<sub>2</sub>O<sub>3</sub> was used as a marker of the ME-controlled antiferromagnetic (AFM) order parameter. The interfacial exchange coupling between FM and AFM spins results in the exchange bias<sup>16-18</sup> and the exchange bias polarity is, in principle, determined by the

interfacial AFM spin direction. Based on this fundamental, they demonstrated that the exchange bias polarity could be reversed by the so-called ME-field cooling (MEFC) method. In this scenario, to switch the exchange bias polarity, temperature increase was necessary, that is, the system was required to be initialized by heating the sample above the Néel temperature. In 2010, He *et al.*<sup>19</sup> developed this technique in the isothermal mode. However, these two studies adopted the bulk Cr<sub>2</sub>O<sub>3</sub> substrate, and thus the realization of the ME effect in the *all-thin-film* system, which is essential to the device application, was challenging.

Before the achievement of the ME effect through the Cr<sub>2</sub>O<sub>3</sub> thin film, some studies theoretically analyzed surface magnetization<sup>20</sup> (or boundary magnetization<sup>21</sup>). It was supposed that the ME switching of the exchange bias polarity was due to the electrically controllable boundary magnetization that coupled with the AFM order parameter<sup>19,21</sup>. In 2014, we presented the experimental evidence of the boundary magnetization on Cr<sub>2</sub>O<sub>3</sub>(0001)<sup>22</sup> including the roughness-insensitive magnetization, absence of the training effect of exchange bias, and ME switching. Nowadays, owing to the achievement of both the MEFC<sup>22-24</sup> and isothermal switching<sup>25-28</sup> in an *all-thin-film* system, we can access the details of the ME switching such as the energy condition of the switching<sup>27</sup> and switching dynamics<sup>28</sup>. In this paper, we review the recent progress of the ME control of the AFM domain state of Cr<sub>2</sub>O<sub>3</sub>, mainly based on our own results as the subject of the magnetic society of Japan (MSJ) outstanding research award 2017.

## 2. Magnetoelectric control of AFM Cr<sub>2</sub>O<sub>3</sub> domain state

In Cr<sub>2</sub>O<sub>3</sub>, the Cr<sup>3+</sup> spin lies along the  $c$  axis, and the spin direction is contradictory at the neighbored  $c$  plane (Fig. 1). According to this spin alignment, Cr<sub>2</sub>O<sub>3</sub>(0001) thin film is suitable for inducing the perpendicularly-directed exchange bias that meets the recent requirement of the spintronic devices. In reality, a high perpendicular exchange magnetic anisotropy  $K$  above 0.4 mJ/m<sup>2</sup> was reported, which can be altered using

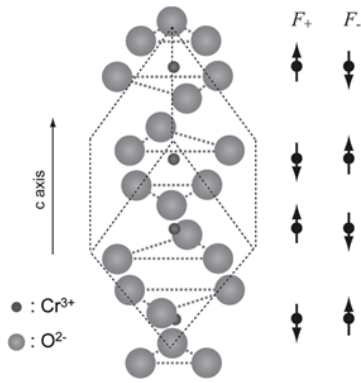


**Fig. 1** Crystal structure and spin alignment of  $\text{Cr}_2\text{O}_3$

different underlayers by alternating the crystal parameters (the lattice parameters and specific ion positions of  $\text{Cr}^{3+}$  and  $\text{O}^{2-}$  ion)<sup>29</sup>. Furthermore, in contrast to the fact that the coercivity enhancement is sometimes accompanied with the exchange bias, the coercivity enhancement of the FM/ $\text{Cr}_2\text{O}_3$  stacked film can be suppressed using a suitable spacer layer at the FM/ $\text{Cr}_2\text{O}_3$  interface<sup>30</sup>. Details about the exchange bias can be found in some previous reviews<sup>16-18</sup> and, in particular that about the perpendicular exchange bias using a  $\text{Cr}_2\text{O}_3(0001)$  film can be found in our previous review<sup>31</sup>, respectively.

According to the above-mentioned spin alignment, two magnetic domains with the opposite  $\text{Cr}^{3+}$  spins are energetically degenerated (Fig. 1). The free energy of the two domains under both electric field  $E$  and magnetic field  $H$  is expressed by<sup>32</sup>

$$F_{\pm} = F_0 + \sigma_i H_i + \rho_i E_i + 1/2 \chi_{ij} H_i H_j + 1/2 \chi'_{ij} E_i E_j \pm \alpha_{ij} E_j H_i + \dots \quad (1)$$

where the first term ( $F_0$ ) is a constant;  $\sigma_i$  and  $\rho_i$  are pyromagnetic and pyroelectric coefficients, respectively;  $\chi_{ij}$  and  $\chi'_{ij}$  are magnetic and dielectric susceptibility, respectively; and  $\alpha_{ij}$  is the ME coefficient. The second and third terms represent the pyromagnetism and pyroelectric polarizations, respectively, which can be eliminated for  $\text{Cr}_2\text{O}_3$  because of its crystallographic symmetry.<sup>32</sup> The fourth and fifth terms represent the magnetization and electric polarization, respectively, and the sixth term represents the ME effect. The sign of the sixth term depends on the AFM order parameter of the two AFM domains.  $F_+$  and  $F_-$  denote the free energies of the two domains. Equation (1) indicates that the energy difference of

$$\Delta F = 2\alpha_{ij} E_i H_j \quad (2)$$

was generated for the two domains by simultaneously applying the electric  $E$  and magnetic  $H$  fields, i.e., the degeneration was broken. Consequently, two AFM

domains become selectable. Since the exchange bias of the film is determined by the AFM domain state<sup>33,34</sup> and is controllable by the ME effect. Till date, two types of ME-induced switching protocols have been proposed: MEFC and isothermal processes. In the following section, we describe the results for each process.

## 2.1 MEFC process

MEFC is a cooling method in which the magnetic and electric fields are simultaneously applied during the cooling from above the Néel temperature of  $\text{Cr}_2\text{O}_3$  (~307 K)<sup>10,35</sup>. In this process, the AFM domain state is determined by the energy competition between the interfacial exchange coupling and ME effect on the onset of the AFM ordering. When electric field  $E$  is below the threshold value, the interfacial exchange coupling dominates the AFM domain state, and the exchange bias polarity is then determined by the magnetic field (more precisely, the FM spin direction) during the cooling. This situation is similar to the conventional field-cooling (FC) process. In contrast, when electric field  $E$  exceeds the threshold value, the energy gain due to the ME effect, proportional to the product of  $E$  and  $H$  ( $EH$  product, see eq. (2)) overcomes the interfacial exchange coupling energy. As a result, the exchange bias polarity is the opposite of that obtained in the previous case.

As a model system to assess the above-mentioned argument, we adopted the Pt/Co(Pt)/ $\text{Cr}_2\text{O}_3$ /Pt thin film exhibiting a perpendicular exchange bias. The details of the film fabrication and the structural details can be found in refs. 29 and 30. To detect the exchange bias polarity, we measured the magnetization curve based on the anomalous Hall effect (AHE) measurements using

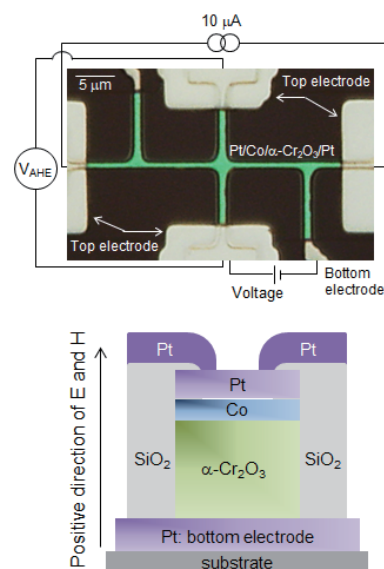


**Fig. 2** Optical microscope image of the micro-fabricated Hall device with the measurement setup. The bottom image represent the schematic drawing of the cross-sectional view of the device.<sup>24</sup>



the micro-fabricated device. The optical microscope image of the typical Hall device with the equivalent circuit is shown in Fig. 2. In this device, the Pt buffer layer and the FM layer acted as the bottom and the top electrodes, respectively. In this setup, the electric field was applied across the  $\text{Cr}_2\text{O}_3$  layer. The positive directions of magnetic and electric fields were defined as the direction from the bottom electrode to the top electrode. For the identical device used for the AHE measurements, the leakage current was also evaluated. At 312 K and 2000 kV/cm, the leakage current was the order of  $1 \text{ A/cm}^2$  which is sufficiently low to rule out the current-induced switching.

Fig. 3(a) shows the AHE loops after the MEFC. Note that the AHE loops were measured at the highest magnetic

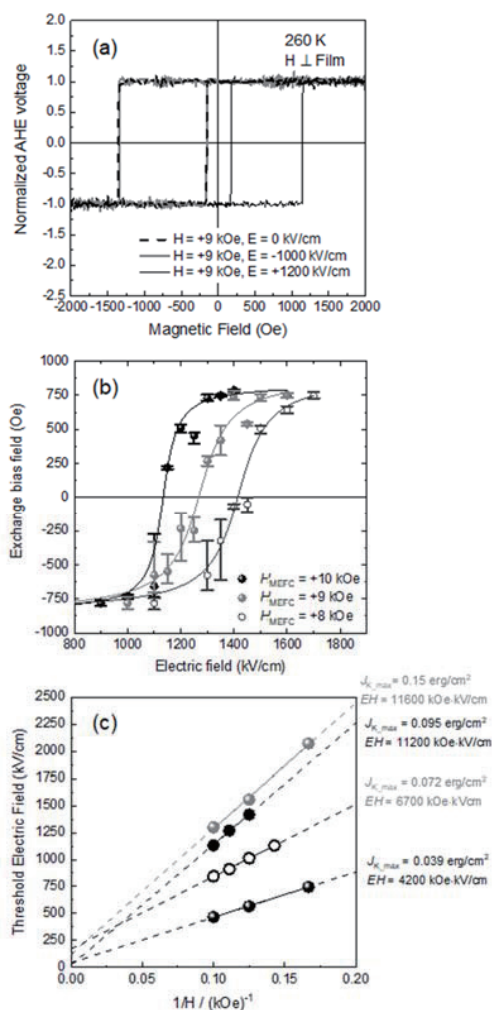


**Fig. 3** (a) Typical AHE loops after MEFC with positive (gray dotted) and negative (black solid)  $EH$  field.<sup>24)</sup> Film used was the Pt/Co/Pt/ $\text{Cr}_2\text{O}_3$ /Pt film. (b) Change in the exchange bias field with applied  $E$  during the MEFC for the Pt/Co/ $\text{Cr}_2\text{O}_3$ /Pt film. The applied  $H$  during the MEFC was +10 kOe (black, closed circle), +9 kOe (gray, closed circle), and +8 kOe (black, open circle).<sup>30)</sup> (c) Change in  $E_{\text{th}}$  with the inverse  $H$  for some films with different  $J_K$ .<sup>30)</sup>

field  $H$  of  $\pm 2 \text{ kOe}$  and zero electric field  $E$ , and thus the AFM domain switching cannot occur during the AHE measurements. The negative exchange bias was observed for both the FC process with  $H = +10 \text{ kOe}$  (black dotted) and the MEFC process with  $H = +10 \text{ kOe}$  and  $E = -1000 \text{ kV/cm}$  (gray solid).<sup>24)</sup> Considering that Co and Cr spins are antiferromagnetically coupled at the interface,<sup>36)</sup> the positive magnetic field favors the upward Co moment and the downward interfacial Cr moment. Since the interfacial Cr moment, i.e., as the boundary magnetization couples with the AFM order parameter, a negative  $EH$  also favors the downward Cr moment. Consequently, when  $EH \leq 0$ , the above-mentioned energy competition, and thus the switching of the exchange bias polarity, does not occur. However, when a positive  $EH$  was applied, the upward interfacial Cr moment is energetically favorable. When the value of  $EH$  is high enough to overcome the interfacial exchange coupling, the interfacial Cr moment should be upward, consequently leading to a positive exchange bias. As shown by the black solid line in Fig. 3(a), the AHE loop after the MEFC with  $H = +10 \text{ kOe}$  and  $E = +1200 \text{ kV/cm}$  represents the positive exchange bias, which agrees with the above-mentioned arguments.

As long as the exchange bias polarity is determined by the energy competition, there should be a threshold condition to switch the exchange bias polarity. Fig. 3(b) shows the change in the exchange bias field  $H_{\text{EX}}$  with respect to the electric field  $E$  during the MEFC with a constant magnetic field  $H$ . The sign of the exchange bias changes from negative to positive with increasing  $E$ . The change in  $H_{\text{EX}}$  with  $E$  can be represented by the functional form of  $\tanh(\Delta G)$ , where  $\Delta G$  represents the energy difference between negative and positive exchange-biased states. This agrees with the previous energetic interpretation to induce the positive exchange bias in Fe/FeF<sub>2</sub> system by using the conventional FC process in which the energy competition between the interfacial exchange coupling and Zeeman energy in FeF<sub>2</sub> layer was considered.<sup>37)</sup> This analogy can be understood through eq. (2), which represents the Zeeman energy of the  $E$ -induced magnetization ( $\alpha_{ij}\vec{E}$ ) based on the magnetic field  $H$ .

When defining the threshold electric field  $E_{\text{th}}$  at which the exchange bias is zero,  $E_{\text{th}}$  increases with decreasing  $H$  during the MEFC. As shown in Fig. 3(c),  $E_{\text{th}}$  is inversely proportional to  $H$ , as shown by eq. (2). The slope of the  $E_{\text{th}}-1/H$  relationship yields the required  $EH$  product to switch the exchange bias polarity,  $(EH)_{\text{th}}$ . According to the above-mentioned arguments, the  $(EH)_{\text{th}}$  value increases with the interfacial exchange coupling. Although the direct determination of the interfacial exchange coupling energy is difficult,  $J_K$  is a measure of the exchange coupling energy. Fig. 3(c) shows the  $E_{\text{th}}-1/H$  relationship for some films with different  $J_K$  values.<sup>31)</sup> The slope of the curve increases with  $J_K$ , thus supporting the earlier discussion.

## 2.2 Isothermal process

Although the switching based on the MEFC process requires temperature hysteresis, the temperature change is not involved in the isothermal switching. In addition, we can obtain additional information, such as the reversibility of the switching<sup>27)</sup> and the dynamics of the ME-induced switching<sup>28)</sup>, which could help with the full understanding of ME switching. This section presents the results for the Pt/Co/Au/Cr<sub>2</sub>O<sub>3</sub>/Pt stacked film, in which the Au spacer layer was deposited to tune the interfacial exchange coupling strength and interfacial magnetic anisotropy<sup>30)</sup>.

### 2.2.1 Static switching using DC voltage

First, we discuss the reversible switching of the perpendicular exchange bias. Iyama and Kimura<sup>39)</sup> reported that Cr<sub>2</sub>O<sub>3</sub> showed a clear hysteresis in both the  $M$ - $H$  curve under constant electric field  $E$  and the  $P$ - $E$  curve under constant magnetic field  $H$ : a ferromagnetic (ferroelectric) feature under constant  $E$  ( $H$ ). This implies that the magnetic domain state of Cr<sub>2</sub>O<sub>3</sub> is switchable in an isothermal manner. As the exchange bias polarity couples with the AFM domain state through boundary magnetization, hysteresis also occurs with the change in  $H_{EX}$  and  $E$  under constant  $H$ , as shown in Fig. 3(a). This is contrastive to the MEFC process in which the interfacial Cr<sup>3+</sup> orientation is affected by the above-mentioned energy competition. We obtained different  $E_{th}$  values of  $H_{EX}$  for the positive-to-negative (P-to-N) and the negative-to-positive (N-to-P) switchings. The difference in  $E_{th}$  should be due to the unidirectional nature of the interfacial exchange coupling at the FM/AFM interface. The sign of the switching direction denotes the exchange bias polarity. Here, we discuss the energy condition of the isothermal switching. The magnetic free energy of the oppositely directed AFM domains per unit area for the FM/Cr<sub>2</sub>O<sub>3</sub> exchange-coupled system can be expressed as

$$\begin{aligned}
 F &= K_{AFM} t_{AFM} \sin^2 \theta - \alpha_{33} E H t_{AFM} \cos \theta \\
 &\quad - M_{AFM} H \cos \theta - J S_{FM} S_{AFM} \cos \theta \\
 &= K_{AFM} t_{AFM} \sin^2 \theta \\
 &\quad - (\alpha_{33} E t_{AFM} + M_{AFM}) H \cos \theta \\
 &\quad - J S_{FM} S_{AFM} \cos \theta
 \end{aligned} \quad (3)$$

where  $K_{AFM}$  is the magnetic anisotropy energy density of the AFM layer,  $t_{AFM}$  is the AFM layer thickness,  $\alpha_{33}$  is the ME coefficient,  $J$  is the interfacial exchange coupling energy,  $S_{FM}$  and  $S_{AFM}$  are the FM and AFM spins, respectively, and  $M_{AFM}$  is the uncompensated AFM moment. Further,  $\theta$  is denoted by the angle between the interfacial AFM and FM spins (or  $H$ ). The first, second, and third terms represent the magnetic anisotropy energy, Zeeman energy of the  $E$ -induced magnetization and uncompensated AFM spin, and the interfacial exchange coupling, respectively.  $M_{AFM}$  can be caused by the defect-induced finite magnetization<sup>40)</sup> and/or the interfacial uncompensated AFM moment, which was the dominant factor in our case.<sup>27)</sup> Note that in eq. (3), the FM spins are fixed to the direction of magnetic field  $H$  because the applied magnetic field  $H$  during the application of electric field  $E$  is high enough ( $> 40$  kOe) to

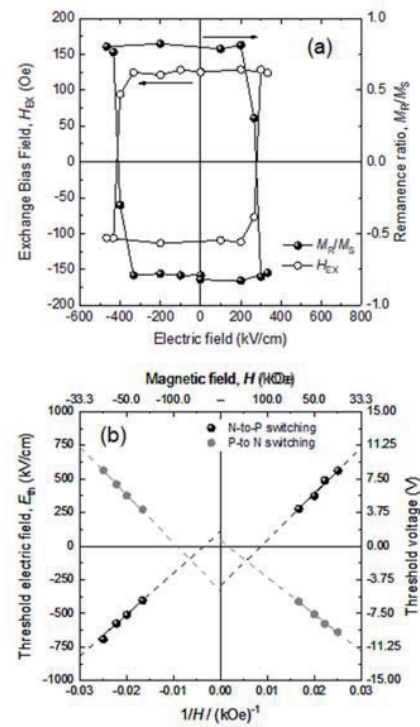


**Fig. 4** (a) Changes of  $H_{EX}$  (left axis) and  $M_r/M_s$  (right axis) with  $E$  measured at 280 K. (b) Change of  $E_{th}$  as a function of  $1/H$  for both N-to-P (solid) and P-to-N (open) switchings.<sup>27)</sup>

fix the FM spin. Thus, the Zeeman energy and magnetic anisotropy energy of the FM layer are not included in eq. (3) because these terms become constant when the FM magnetization is fixed. By minimizing eq. (3), the energy condition for ME switching is derived as<sup>27)</sup>

$$\left( \alpha_{33} E + \frac{M_{AFM}}{t_{AFM}} \right) H = \pm 2 K_{AFM} - \frac{J S_{FM} S_{AFM}}{t_{AFM}} \quad (4)$$

Each sign of the first term corresponds to the N-to-P and P-to-N switchings. Fig. 3(b) shows the magnetic field dependence of  $E_{th}$ , which is inversely proportional to  $H$ , as shown in eq. (4).

The unique feature that appeared in the all-thin-film system was (1) the different switching energy depending on the switching direction and (2) the appearance of the offset  $E$  in the  $E$ - $1/H$  relationship. The former is found in the difference in the slope of two curves, i.e. N-to-P switching and P-to-N switching. Accordingly, the slopes of the two curves give  $K_{AFM}$  and  $J S_{FM} S_{AFM}$ , whose values are  $4.5 \pm 0.6 \times 10^3$  J/m<sup>3</sup> and  $1.5 \pm 0.2 \times 10^{-2}$  mJ/m<sup>2</sup>, respectively, assuming  $\alpha_{33} = 3$ –4 ps/m. The estimated  $K_{AFM}$  is approximately half of the  $K_{AFM}$  of the bulk Cr<sub>2</sub>O<sub>3</sub> at the measurement temperature of 280 K. This underestimation is probably because the above-mentioned estimation assumes the coherent rotation, while in reality, the nucleation and propagation of the reversed AFM domains should be involved<sup>26)</sup>. In addition, the estimated value of  $J S_{FM} S_{AFM}$  differs from that of the ideal model. That is, the estimated  $J S_{FM} S_{AFM}$  was

approximately twice of the exchange anisotropy energy density,  $J_K = H_{EX} \cdot M_S \cdot t_{FM} = 5.8 \times 10^{-3} \text{ mJ/m}^2$ . The values of  $J_{S_{FM}S_{AFM}}$  and  $J_K$  might be equal when the pinned spin model<sup>41)</sup> is valid in our film. However, in actuality, the interfacial Cr moments were not perfectly pinned but canted from the original direction with respect to the FM magnetization reversal,<sup>36)</sup> which obviously deviates from the pinned spin model.

The offset  $E$  in the  $E$ - $1/H$  relationship, i.e., the nonzero  $E_{th}$  interception in the limit of  $1/H$  to zero is another

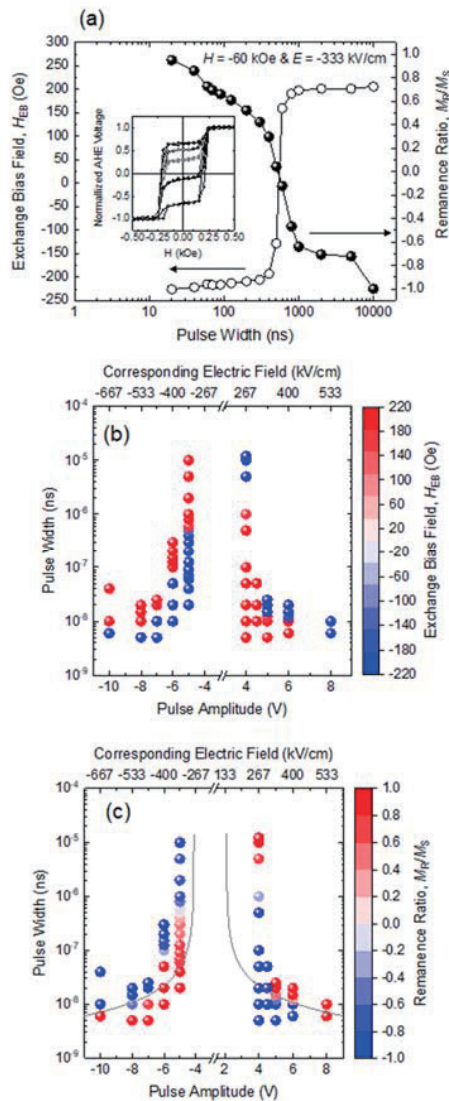


**Fig. 5** (a) Changes in  $H_{EX}$  and  $M_R/M_S$  as a function of pulse width.  $H_{EX}$  and  $M_R/M_S$  were collected from the AHE loops after applying pulsed  $E$  under the constant  $H$  ( $= -60 \text{ kOe}$ ). The pulse amplitude was  $-333 \text{ kV/cm}$ . Inset of (a) represents the typical AHE loop at the intermediate state. Changes in (b)  $H_{EX}$  and (c)  $M_R/M_S$  as functions of pulse amplitude and width, with white/black circles representing positive/negative values and their color depth representing absolute values. Solid line in (c) represents the calculated switching time. Measurement temperature was  $280 \text{ K}$ .<sup>28)</sup>

characteristics of all-thin-film system. According to eq. (3), the offset  $E_{th}$  is caused by the uncompensated AFM moment  $M_{AFM}$ . In our system,  $M_{AFM}$  relevant to the offset  $E_{th}$  is mainly the interfacial uncompensated AFM moment. This should be reasonable because the ME switching of the AFM domain detected through the exchange bias is an interfacial effect. In other words, by utilizing  $E_0$  positively, the shift of the  $E$ - $1/H$  curve from the origin becomes significant. In the practical use,  $E_{th}$  at the certain  $H$  decreases with increasing  $E_0$ , i.e. increasing  $M_{AFM}$ <sup>40,42)</sup> or decreasing  $t_{AFM}$  which may become one solution to decrease the switching energy.

## 2.2.2 Dynamical switching using pulse voltage

The important advantage of isothermal switching is that we can access the switching dynamics by adopting the pulsed magnetic or electric fields. In general, the pulse width of the pulsed magnetic field above several tens of kOe is in the range of milliseconds.<sup>43)</sup> In contrast, the fast pulse  $E$  below microseconds can be easily generated using the general pulse generator. Thus, we can access fast dynamics by adopting the pulsed electric field and a constant magnetic field. Figure 4(a) shows the change in  $H_{EX}$  and  $M_R/M_S$  as a function of pulse width; these factors were collected from the AHE loops after applying  $H = -60 \text{ kOe}$  and pulsed electric field with the amplitude of  $-333 \text{ kV/cm}$  and width of  $20 \text{ ns} - 10 \mu\text{s}$ .<sup>28)</sup> As the DC  $E_{th}$  value of this film was  $-275 \text{ kV/cm}$  ( $-4.1 \text{ V}$ ; see reference 28), the above-mentioned condition is slightly above the DC threshold condition. With increasing pulse width,  $H_{EX}$  ( $M_R/M_S$ ) changes from negative (positive) to positive (negative) at the pulse width of  $500 \text{ ns}$ . The change in  $M_R/M_S$  is gradual compared with that in  $H_{EX}$ . This is because the coercivity  $H_C$  is lower than  $H_{EX}$ , the magnetization reversal is sharp around  $H_C$ , and the two-step magnetization process was observed at the intermediate state, as shows in the inset of Fig. 4(a). The slow switching time suggests that the switching process is dominated by the domain wall motion. In such a case, the switching time is dominated by the domain wall velocity and could be decreased by increasing the pulse amplitude. Figures 4(b) and 4(c) show the change of  $H_{EX}$  and  $M_R/M_S$  as functions of pulse amplitude and pulse width, respectively. The magnetic field during the application of an electric field was maintained at  $-60 \text{ kOe}$ . The switching time decreases with increasing pulse amplitude, as expected earlier. As the ME-induced switching is triggered by the electric field, the microscopic origin of the domain wall motion might be different from the magnetic-field induced domain wall dynamics observed in the ordinal FM layer.<sup>44-46)</sup> Nonetheless, as indicated by eqs. (1) and (2), the role of electric field  $E$  is to induce magnetization, and a change in  $E$  alters the energy gain by the Zeeman energy of the  $E$ -induced magnetization. Therefore, the driving force to induce the magnetic domain wall propagation should be analogous to the case of FM (or ferrimagnetic) domain wall. By assuming that  $\text{Cr}_2\text{O}_3$  under a finite  $E$  behaves as a ferrimagnet,<sup>32)</sup> the domain wall velocity was calculated based on the simple theory discussed in refs. 44-47. The details of the calculation can be found in ref. 28. As shown by the solid line in Fig. 4(c), the switching time can be roughly reproduced using the simple model with some assumed values: domain wall width,  $38 \text{ nm}$ <sup>48)</sup>; ME



coefficient at 280 K, 3.5 ps/m<sup>49</sup>); Gilbert damping parameter of each sublattice, 0.05; and travel distance, 1 μm (half of the Hall device width). Despite the rough agreement in the switching times, some assumed values need further investigation. For instance, the assumed Gilbert damping parameter of each sublattice is the order of 10<sup>-2</sup>–10<sup>-1</sup>, which may be larger than the predicted value.<sup>48</sup> One reason may be the creep motion of the domain wall under our adopted experimental condition as indicated by the large deviation in the low amplitude regime. The direct observation of the ME-induced magnetization reversal process is beneficial for both the quantitative analysis and deeper understanding of the phenomena.

### 3. Element-specific magnetic domain observation

For the observation of the ME-induced magnetization switching process, it can be simply assumed that FM and AFM domains are coupled spatially, at least, at the remanent state. In other words, if this assumption is valid, we can obtain the AFM domain pattern by observing the FM domain. However, this is nontrivial. In the case of the in-plane exchange-biased film, the AFM domains can be imaged through X-ray linear dichroism (XMLD).<sup>50,51</sup> Accordingly, the AFM domain just below the individual FM domains is not a single domain state, implying that FM and AFM domain patterns are not the same. Hence, as a first step in the investigation, the magnetic domain states of FM and AFM layers must be obtained independently.

The XMLD technique is not applicable for our system because the AFM spin orientation should be restricted to upward or downward directions (see Fig. 1), and such collinear spins are not distinguishable through XMLD. X-ray magnetic circular dichroism (XMCD) complements this limitation and is a powerful tool for the perpendicularly directed spin system. Based on the XMCD measurements by using the focused soft X-ray, we observed the spatial distribution of the XMCD intensity corresponding to the magnetic domains for FM Co and AFM Cr spins independently.<sup>33</sup> In this work, we employed the scanning XMCD microscope equipped at BL25SU, SPring-8. The schematic drawing of the

scanning XMCD microscope is shown in Fig. 6. In this microscope, the soft X-ray was focused on the sample using the Fresnel Zone Plate (FZP) and the order sorting aperture (OSA). By scanning the sample in *x* and *y* directions in keeping the focused state, the special distribution of the XMCD intensity was collected. In this microscope, the XMCD signal can be detected based on the surface-sensitive total electron yield method, suitable to detect the tiny signal from the interfacial uncompensated Cr spin. The details of this microscope can be found in refs. 33 and 52.

Figure 7 shows the spatial distributions of XMCD of Co and Cr for the Pt/Co/Cr<sub>2</sub>O<sub>3</sub>/Pt thin film measured at 205 K. The multidomain state was created through AC-demagnetization at room temperature, and then the

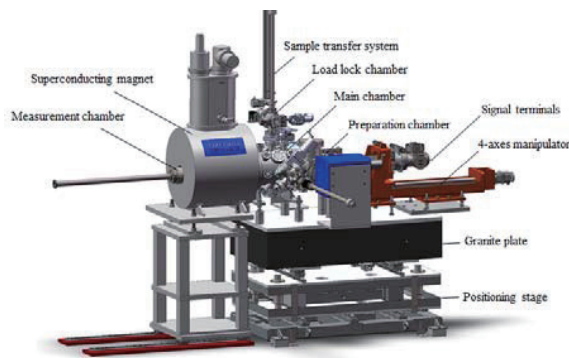


**Fig. 6** Schematic drawings of the scanning XMCD microscope. [Courtesy to Dr. Nakamura and Dr. Kotani of JASRI] Details about the optical setup, the scanning method et al should be referred to ref. 52.

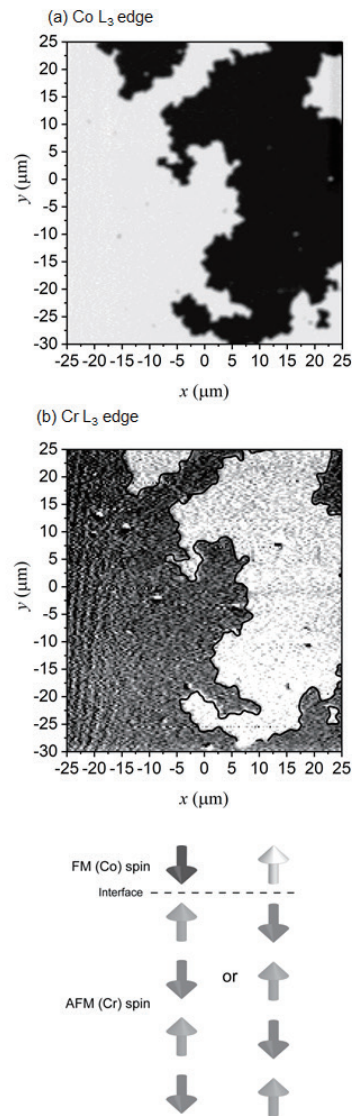


**Fig. 7** Spatial distribution of XMCD measured at 205 K. Photon energy used for the imaging was (a) 778 eV (Co *L*<sub>3</sub> edge) and (b) 576 eV (Cr *L*<sub>3</sub> edge). Colors correspond to spin orientations schematically shown at bottom. Black solid line in (b) represents the domain boundary of the oppositely directed FM domains<sup>33</sup>

sample was cooled to retain the demagnetized state. Note that the XMCD from the Cr was performed using the interfacial uncompensated Cr moment. Two patterns were observed to be very similar indicating that the FM and AFM domains are spatially coupled. This spatial coupling of the magnetic domains is probably due to the strong interfacial exchange coupling and the collinear interfacial spin alignments of both Co and Cr. The sign of the XMCD is contradictory for Co and Cr indicating antiferromagnetic interfacial exchange coupling.<sup>36)</sup> From the spatial coupling of the magnetic domains, the exchange bias polarity can be assumed to be determined according to the domain-by-domain basis, implying that the exchange bias polarity is determined by the interfacial AFM moments, i.e., the boundary magnetization. This can be directly verified by measuring the local magnetization curve on the individual magnetic domains; this is under investigation. For the direct observation of the ME-induced magnetization switching process, in addition to the imaging technique described previously, the applications of magnetic field above several tens of kOe and the electric field (of both DC and pulse) in the microscope instrument are necessary. These techniques are now in the developing stage and will be reported in the near future.

#### 4. Summary

In this article, we reviewed the ME-induced magnetization reversal mainly based on our own results. Discovered in the 1950s in bulk Cr<sub>2</sub>O<sub>3</sub>, the ME effect was recently observed in an all-thin-film system. Owing of this development, we could address the various phenomena involving the ME effect, e.g., the control of the interfacial magnetization and switching dynamics. Many challenges still exist for the actual application of the ME effect to a storage/memory device, e.g., the reduction of the switching energy, fast switching, and thermal stability. To solve these challenges, a deeper understanding of the ME-induced phenomena is essential.

**Acknowledgements** Part of this work was conducted by collaborating with Dr. Tetsuya Nakamura, Dr. Motohiro Suzuki, Dr. Yoshinori Kotani, Dr. Kentaro Toyoki (JASRI), Dr. Chiharu Mitsumata (NIMS), Dr. Tatsuo Shibata, and Dr. Shogo Yonemura (TDK corp.). This work was partly supported by JSPS KAKENHI (Grant Nos. 16H03832, 16H02389), the ImPACT program of Council for Science, Technology and Innovation (Cabinet Office, Government of Japan), and the Photonics Advanced Research Center (PARC) at Osaka University.

#### References

- 1) P. Curie: *J. Phys. (Paris)*, **3**, 393 (1894).
- 2) A. Perrier: *Arch. Sci. Phys. Nat.*, **4**, 369 (1922).
- 3) A. Perrier and A. J. Starling: *Arch. Sci. Phys. Nat.*, **4**, 373 (1922), *ibid.* **5**, 333 (1923).
- 4) A. Perrier and C. E. Borel: *Arch. Sci. Phys. Nat.*, **7**, 289 (1925).
- 5) A. Piccard: *Arch. Sci. Phys. Nat.*, **6**, 404 (1924).
- 6) P. Debye: *Z. Phys.*, **36**, 300 (1926).
- 7) J. H. Van Vleck: *The theory of electric and magneto susceptibilities* (Oxford University Press, London, 1932), pp.113-121 and pp. 279-281.
- 8) L. D. Landau and E. M. Lifshitz, *Electrodynamics of continuous media* (English Transl. Pergamon Press, Oxford, 1960), p. 115, p.119, pp.313-344.
- 9) I. E. Dzyaloshinskii: *Sov. Phys. JETP*, **10**, 628 (1959).
- 10) D. N. Astrof: *Sov. Phys. JETP*, **11**, 708 (1960).
- 11) V. J. Folen, G. T. Rado, and E. W. Stadler: *Phys. Rev. Lett.*, **6**, 607 (1961).
- 12) T. Arima: *J. Phys. Soc. Jpn.*, **80**, 052001 (2011).
- 13) T. H. O'Dell, *The electrodynamic of magneto-electric media* (North-Holland Publishing Company, 1970), Chapter 1.
- 14) M. Fiebig: *J. Phys. D: Appl. Phys.*, **38**, R123 (2005).
- 15) P. Borisov, A. Hochstrat, X. Chen, W. Kleemann, and C. Binek: *Phys. Rev. Lett.*, **94**, 117203 (2005).
- 16) J. Nogués and I. K. Schuller, *J. Magn. Magn. Mater.*, **192**, 203 (1999).
- 17) A. E. Berkowitz and K. Takano: *J. Magn. Magn. Mater.*, **200**, 553 (2000).
- 18) R. L. Stamps: *J. Phys. D: Appl. Phys.*, **33**, R247 (2000).
- 19) X. He, Y. Wang, A. N. Caruso, E. Voscovo, K. D. Bealshchenko, P. A. Dowben, and C. Binek: *Nat. Mater.*, **9**, 579 (2010).
- 20) A. F. Andreev, *JETP Lett.*, **63**, 758 (1996).
- 21) K. D. Belashchenko: *Phys. Rev. Lett.*, **105**, 147204 (2010).
- 22) K. Toyoki, Y. Shiratsuchi, T. Nakamura, C. Mitsumata, S. Harimoto, Y. Takechi, T. Nishimura, H. Nomura, and R. Nakatani: *Appl. Phys. Express*, **7**, 114201 (2014).
- 23) T. Ashida, M. Oisa, N. Shimomura, T. Nozakim T. Shibata, and M. Sahashi: *Appl. Phys. Lett.*, **104**, 152409 (2014).
- 24) K. Toyoki, Y. Shiratsuchi, A. Kobane, S. Harimoto, S. Onoue, H. Nomura, and R. Nakatani: *J. Appl. Phys.*, **117**, 19D902 (2015).
- 25) T. Ashida, M. Oida, N. Shimomura, T. Nozaki, T. Shibata, and M. Sahashi: *Appl. Phys. Lett.*, **106**, 132407 (2015).
- 26) K. Toyoki, Y. Shiratsuchi, A. Kobane, C. Mitsumata, Y. Kotani, T. Nakamura, and R. Nakatani: *Appl. Phys. Lett.*, **106**, 162494 (2015).
- 27) T. V. A. Nguyen, Y. Shiratsuchi, A. Kobane, S. Yoshida, and R. Nakatani: *J. Appl. Phys.*, **122**, 073905 (2017).
- 28) T. V. A. Nguyen, Y. Shiratsuchi, and R. Nakatani: *Appl. Phys. Express*, **10**, 083002 (2017).
- 29) Y. Shiratsuchi, Y. Nakano, N. Inami, T. Ueno, K. Ono, R. Kumai, R. Sagayama, and R. Nakatani: *J. Appl. Phys.*, **123**, 103903 (2018).
- 30) Y. Shiratsuchi, W. Kuroda, T. V. A. Nguyen, Y. Kotani, K. Toyoki, T. Nakamura, M. Suzuki, K. Nakamura, and R. Nakatani: *J. Appl. Phys.*, **121**, 073902 (2017).
- 31) Y. Shiratsuchi, and R. Nakatani: *Mater. Trans.*, **57**, 781 (2016).
- 32) T. J. Martin, and J. C. Anderson: *IEEE Trans. Magn.*, **2**, 446 (1966).
- 33) Y. Shiratsuchi, Y. Kotani, S. Yoshida, Y. Yoshikawa, K. Toyoki, A. Kobane, R. Nakatani, and T. Nakamura: *AIMS Mater. Sci.*, **2**, 484 (2015).
- 34) Y. Shiratsuchi, S. Watanabe, H. Yoshida, N. Kishida, R. Nakatani, Y. Kotani, K. Toyoki, and T. Nakamura: to be submitted.
- 35) T. G. MacGuire, E. J. Scott, and F. H. Grannis: *Phys. Rev.*, **102**, 1000 (1956).
- 36) Y. Shiratsuchi, H. Noutomi, H. Oikawa, T. Nakamura, M. Suzuki, T. Fujita, K. Arakawa, Y. Takechi, H. Mori, T. Kinoshita, M. Yamamoto, and R. Nakatani: *Phys. Rev. Lett.*, **109**, 077202 (2012).
- 37) B. Kagerer, Ch. Binek, and W. Kleemann: *J. Magn. Magn. Mater.*, **217**, 139 (2000).
- 38) K. Toyoki, Y. Shiratsuchi, A. Kobane, S. Harimoto, S. Onoue, H. Nomura, and R. Nakatani: *J. Appl. Phys.*, **117**, 19D902

- (2015).
- 39) A. Iyama, and T. Kimura: *Phys. Rev. B*, **87**, 180408(R) (2013).
- 40) T. Kosub, M. Koppe, R. Hühne, P. Appel, B. Shields, P. Maletinsky, R. Hübner, M. O. Liedke, J. Fassbender, O. G. Schmidt, and D. Makarov: *Nat. Comm.*, **8**, 13985 (2017).
- 41) W. H. Meiklejohn, and C. P. Bean: *Phys. Rev.*, **102**, 1413 (1956), *ibid* **105**, 904 (1957).
- 42) M. Al-Mahdawi, S. P. Pati, Y. Shiokawa, S. Ye, T. Nozaki, and M. Sahashi: *Phys. Rev. B*, **95**, 144423 (2017).
- 43) T. Nakamura, Y. Narumi, T. Hirono, M. Hayashi, K. Kodama, M. Tsunoda, S. Isogami, H. Takahashi, T. Kinoshita, K. Kindo, and H. Nojiri: *Appl. Phys. Express*, **4**, 066602 (2011).
- 44) T. Ono, H. Miyajima, J. Shigeto, N. Hosoito, and T. Shinjo: *Science*, **284**, 468 (1999).
- 45) D. Atkinson, D. A. Allwood, G. X. Cooke, C. C. Faulkner, and R. D. Cowburn: *Nat. Mater.*, **2**, 85 (2003).
- 46) G. D. Beach, C. Nistor, K. Maxim, and J. K. Erskine: *Nat. Mater.*, **4**, 741 (2005).
- 47) R. Giles, and M. Mascuipur: *J. Mag. Soc. Jpn.*, **15**, 299 (1991).
- 48) K. D. Belashchenko, O. Tedemyshyov, A. A. Kovalev, and O. A. Tretiakov: *Appl. Phys. Lett.*, **108**, 132403 (2016).
- 49) P. Borisov, T. Ashida, T. Nozaki, M. Sahashi, and D. Lederman: *Phys. Rev. B*, **93**, 174415 (2016).
- 50) A. Scholl, J. Stöhr, J. Lüning, J. W. Seo, J. Frompeyrine, H. Siegwark, J. -P. Locquet, F. Nolting, S. Anders, E. E. Fullerton, M. R. Scheinfein, and H. A. Padmore: *Science*, **287**, 1014 (2000).
- 51) F. Nolting, A. Scholl, J. Stöhr, J. W. Seo, J. Frompeyrine, H. Siegwark, J. -P. Locquet, S. Anders, J. Lüning, E. E. Fullerton, M. F. Toney, M. R. Scheinfein, and H. A. Padmore: *Nature*, **405**, 767 (2000).
- 52) Y. Kotani, Y. Senba, K. Toyoki, D. Bikington, H. Okazaki, A. Yasui, W. Ueno, H. Ohashi, S. Hirosawa, Y. Shiratsuchi, and T. Nakamura: *J. Synchrotron Rad.*, **25** in press. <https://doi.org/10.1107/S1600577518009177>.

Received Apr. 30, 2018. Accepted Jul. 24, 2018.

# Understanding Signal-to-Noise Ratio in Heat-Assisted Magnetic Recording

T. Kobayashi, Y. Nakatani\*, and Y. Fujiwara

Graduate School of Engineering, Mie Univ., 1577 Kurimamachiya-cho, Tsu 514-8507, Japan

\*Graduate School of Informatics and Engineering, Univ. of Electro-Communications, 1-5-1 Chofugaoka, Chofu 182-8585, Japan

We improve our model calculation for heat-assisted magnetic recording (HAMR) considering the temperature dependence of the attempt frequency. Then, the signal-to-noise ratio dependence on writing field is calculated for various calculation parameters by employing both our model calculation and the conventionally used micromagnetic calculation. The tendencies of the results of our model calculation and of the micromagnetic calculation are almost the same by this improvement. Therefore, our model calculation can be used for HAMR design. The writing process can be described using the temperature dependences of the grain magnetization reversal probability and the attempt number. If the Gilbert damping constant is small, writing is difficult since the attempt number is small. Write-error can be reduced by reducing the linear velocity, and erasure-after-write can be reduced by increasing the thermal gradient and/or the grain column number.

**Key words:** heat-assisted magnetic recording, signal-to-noise ratio, grain magnetization reversal probability, attempt number

## 1. Introduction

Heat-assisted magnetic recording (HAMR) is a promising candidate as a next generation magnetic recording method beyond the trilemma limit<sup>1)</sup>.

We have already proposed a new HAMR model calculation<sup>2),3)</sup>. The grain magnetization reversal probability and the attempt period, whose inverse is the attempt frequency  $f_0$ , are key physical quantities in our model calculation. We used a constant  $f_0$  value in our previous model calculation. We have also calculated the temperature dependence of  $f_0$ <sup>4)</sup> employing the conventionally used micromagnetic calculation.

In this study, we improve our model calculation considering the temperature dependence of  $f_0$ . Then, we calculate the dependence of the signal-to-noise ratio (SNR) on the writing field for various calculation parameters in HAMR. And we compare the results with those calculated employing the conventionally used micromagnetic calculation at the same time to determine whether our model calculation can be used for HAMR design. Furthermore, we provide the SNR results with physical implications employing our model calculation with a view to HAMR design.

## 2. Calculation Method

### 2.1 Calculation conditions

The medium was assumed to be granular. The writing field switching timing and the calculation conditions are summarized in Fig. 1 (a). The mean grain size  $D_m$ , the standard deviation of the grain size  $\sigma_D/D_m$ , and the grain height  $h$  were 4.9 nm, 10 %, and 8 nm, respectively, and so the grain volume  $V_m$  for  $D_m$  was  $D_m \times D_m \times h = 193 \text{ nm}^3$ . The Curie temperature  $T_c$  and the standard deviation of the Curie temperature  $\sigma_{T_c}/T_c$  were 700 K and 0 %, respectively, since a higher anisotropy constant ratio  $K_u/K_{\text{bulk}}$  is necessary if  $T_c$  is low<sup>5)</sup> where  $K_u/K_{\text{bulk}}$  is the intrinsic ratio of the medium anisotropy constant  $K_u$  to bulk FePt  $K_u$ <sup>6)</sup>. The  $K_u/K_{\text{bulk}}$  value of the medium was 0.4. The calculation parameters were the bit pitch  $D_{\text{BP}}$ , the Gilbert damping constant  $\alpha$ , the thermal gradient  $\partial T/\partial x$  for the down-track direction, and the linear velocity  $v$ .

respectively, since a higher anisotropy constant ratio  $K_u/K_{\text{bulk}}$  is necessary if  $T_c$  is low<sup>5)</sup> where  $K_u/K_{\text{bulk}}$  is the intrinsic ratio of the medium anisotropy constant  $K_u$  to bulk FePt  $K_u$ <sup>6)</sup>. The  $K_u/K_{\text{bulk}}$  value of the medium was 0.4. The calculation parameters were the bit pitch  $D_{\text{BP}}$ , the Gilbert damping constant  $\alpha$ , the thermal gradient  $\partial T/\partial x$  for the down-track direction, and the linear velocity  $v$ .

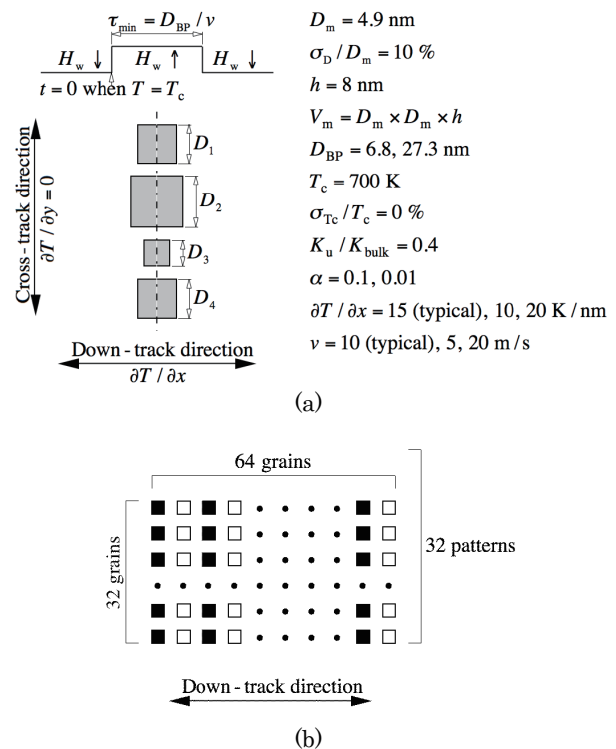


**Fig. 1** (a) Writing field switching timing and calculation conditions, and (b) grain arrangement for signal-to-noise ratio calculation.



We used the damping constants  $\alpha = 0.1$  and  $0.01$  since the value of  $\alpha$  just below  $T_c$  is unknown. Typical values were  $\partial T / \partial y = 15$  K/nm and  $v = 10$  m/s. The thermal gradient  $\partial T / \partial y$  for the cross-track direction was assumed to be 0 K/nm.

$H_w$  and  $\tau_{\min} = D_{BP} / v$  are the writing field and the time available for writing each bit, respectively. The  $H_w$  direction is upward when time  $t$  is  $2n\tau_{\min} \leq t < (2n+1)\tau_{\min}$ , and downward when  $(2n+1)\tau_{\min} \leq t < (2n+2)\tau_{\min}$  where  $n$  is an integer. When  $t = n\tau_{\min}$ , the writing grain temperature  $T$  becomes  $T_c$ . There are fluctuations in the switching timing  $\Delta t$  and position  $\Delta x$  in a granular medium<sup>9)</sup>. However, we assumed  $\Delta t = 0$  and  $\Delta x = 0$  in our discussion of the intrinsic phenomenon.

Figure 1 (b) shows the grain arrangement for the signal-to-noise ratio (SNR) calculation. We used a pattern consisting of 32 grains for the cross-track direction and 64 grains for the down-track direction, and we used 32 patterns for the SNR calculation. One bit consisted of  $32 \times 1$  or  $32 \times 4$  grains, namely one or four grain columns per bit, and  $D_{BP} = 6.8$  or  $27.3$  nm, respectively. An initial magnetization direction, namely upward or downward, is randomly decided.

## 2.2 Model calculation

The magnetization direction of the grains was calculated using the magnetization reversal probability for every attempt time in our model calculation<sup>2)-4)</sup>.

The switching probability  $P_-$  for each attempt where the magnetization  $M_s$  and the writing field  $H_w$  change from antiparallel to parallel is expressed as

$$P_- = \exp(-K_{\beta-}). \quad (1)$$

On the other hand,

$$P_+ = \exp(-K_{\beta+}) \quad (2)$$

is the probability for each attempt where  $M_s$  and  $H_w$  change from parallel to antiparallel. In these equations,

$$K_{\beta-}(T, H_w) = \frac{K_u(T)V}{kT} \left( 1 - \frac{H_w}{H_k(T)} \right)^2 \quad (H_k(T) \geq H_w),$$

$$K_{\beta-}(T, H_w) = 0 \quad (H_k(T) < H_w), \quad (3)$$

and

$$K_{\beta+}(T, H_w) = \frac{K_u(T)V}{kT} \left( 1 + \frac{H_w}{H_k(T)} \right)^2, \quad (4)$$

where  $K_u$ ,  $V$ ,  $k$ ,  $T$ , and  $H_k = 2K_u / M_s$  are the anisotropy constant, the grain volume, the Boltzmann constant, temperature, and the anisotropy field, respectively.

The temperature dependence of  $M_s$  was determined employing a mean field analysis<sup>7)</sup>, and that of  $K_u$  was assumed to be proportional to  $M_s^2$ <sup>8)</sup>. The Curie temperature  $T_c$  can be adjusted by the Cu simple

dilution of  $(\text{Fe}_{0.5}\text{Pt}_{0.5})_{1-z}\text{Cu}_z$ .  $M_s(T_c, T)$  is a function of  $T_c$  and  $T$ .  $M_s(T_c = 770 \text{ K}, T = 300 \text{ K}) = 1000$  emu/cm<sup>3</sup> was assumed.  $K_u(T_c, K_u / K_{\text{bulk}}, T)$  is a function of  $T_c$ , the anisotropy constant ratio  $K_u / K_{\text{bulk}}$ , and  $T$ .  $K_u(T_c = 770 \text{ K}, K_u / K_{\text{bulk}} = 1, T = 300 \text{ K}) = 70$  Merg/cm<sup>3</sup> was assumed. We used  $M_s(T_c = 700 \text{ K}, T)$  and  $K_u(T_c = 700 \text{ K}, K_u / K_{\text{bulk}} = 0.4, T)$  for the calculation in this paper.

On the other hand, the attempt time  $t_k$ , which falls within an attempt period  $\tau_{AP}$ , is determined as follows. The inverse of the attempt period is an attempt frequency  $f_0 = 1 / \tau_{AP}$ . We improve our model calculation considering the temperature dependence of  $f_0$ . We have determined the temperature dependence of  $f_0$ <sup>4)</sup> employing a conventionally used micromagnetic calculation with the Landau-Lifshitz-Gilbert (LLG) equation<sup>9)</sup> where we calculated the temperature dependence of the magnetic properties used in the  $f_0$  calculation with a mean field analysis. The results can be fitted using

$$f_0(T) = \frac{2\alpha}{1+\alpha^2} f_1 \sqrt{\frac{V}{V_m}} \sqrt{\frac{600}{T}} \frac{K_u(T)}{K_u(600 \text{ K})} \quad (5)$$

in consideration of reference 10) where  $f_1 = 500$  (ns)<sup>-1</sup>,  $V_m = 193$  nm<sup>3</sup>, and  $K_u(600 \text{ K}) = 8.0$  Merg/cm<sup>3</sup>. Since there was a very good linear relationship between  $f_0$  and  $T$ , we used

$$f_0(T) = \frac{2a\alpha}{1+\alpha^2} \sqrt{\frac{V}{V_m}} \frac{K_u / K_{\text{bulk}}}{0.4} (T_c - T) \quad (6)$$

instead of Eq. (5) in our calculation where  $a = 5$  (nsK)<sup>-1</sup>. The  $f_0$  value becomes zero at  $T_c$  as shown in Eq. (6).

We defined an initial time  $t_{\text{ini1}}$  at  $T = T_{\text{th}} = 699$  K, which is close to  $T_c = 700$  K, using

$$t_{\text{ini1}} = \frac{T_c - T_{\text{th}}}{(\partial T / \partial x)v} \quad (7)$$

since  $\tau_{AP} = 1 / f_0$  diverges to infinity at  $T = T_c$ . The next initial time  $t_{\text{ini2}}$  can be calculated using the mean attempt period  $\tau_{APm}$  from  $t_{\text{ini1}}$  to  $t_{\text{ini2}}$  expressed by

$$t_{\text{ini2}} - t_{\text{ini1}} = \tau_{APm} = \frac{1}{t_{\text{ini2}} - t_{\text{ini1}}} \int_{t_{\text{ini1}}}^{t_{\text{ini2}}} \tau_{AP}(t) dt. \quad (8)$$

We assumed that the first attempt time  $t_1$  is randomly decided between  $t_{\text{ini1}}$  and  $t_{\text{ini2}}$ . And the attempt time  $t_{k+1}$  ( $k \geq 1$ ) is determined with the following recurrence formula:

$$t_{k+1} - t_k = \tau_{APm} = \frac{1}{t_{k+1} - t_k} \int_{t_k}^{t_{k+1}} \tau_{AP}(t) dt. \quad (9)$$

Figure 2 shows the time dependence of the grain magnetization reversal probability  $P_{\pm}$  for  $t_1 = t_{\text{ini1}}$  and  $t_2 = t_{\text{ini2}}$ . In this paper, figures of  $P_{\pm}$  with time

are shown in the same format. The filled circles indicate the attempt times whose interval is the mean attempt period  $\tau_{APm}$ . The  $f_0$  value is low just below  $T_c$  as shown in Eq. (6), and then  $\tau_{AP} = 1/f_0$  is long just after  $t = 0$  since the time  $t = 0$  corresponds to the writing grain temperature  $T$  becoming  $T_c$ . The temperature decreases with time, and  $\tau_{AP}$  decreases accordingly. Therefore,  $\tau_{APm}$  decreases with time.

The writing field was assumed to be spatially uniform, the direction was perpendicular to the medium plane, and the rise time was zero. Neither the demagnetizing nor the magnetostatic fields were considered during writing since they are negligibly small. The output signal, media noise, and media signal-to-noise ratio (SNR) were calculated using the sensitivity function<sup>11)</sup> of a magnetoresistive head with an element width of 218 nm, a shield-to-shield distance of 15 nm, and a 4.0 nm head-medium spacing. The element width is the same as the cross-track width of the simulation region.

The calculation procedure is described below. First, the medium was characterized by  $T_c = 700$  K,  $K_u/K_{bulk} = 0.4$ , and  $\alpha$ . The grain temperature fell with time from  $T_c$  according to the thermal gradient  $\partial T/\partial x$  along the down-track direction and the linear velocity  $v$ . The attempt times were calculated. The magnetic property and then  $P_{\pm}$  were calculated by undertaking a mean field analysis for every attempt time. The magnetization direction can be determined by the Monte Carlo method for every attempt time. The SNR was obtained from the grain magnetization patterns as shown in Fig. 1 (b).

### 2.3 Micromagnetic calculation

We also calculated the SNR employing a micromagnetic calculation using the LLG equation and compared the results with those obtained employing our model calculation. The calculation conditions for the model calculation and the micromagnetic calculation were the same.

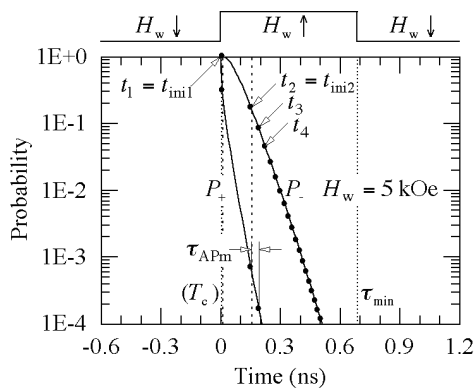


**Fig. 2** Time dependence of grain magnetization reversal probability  $P_{\pm}$  under conditions of 1 column/bit, damping constant  $\alpha = 0.1$ , and typical values. The filled circles indicate the attempt times whose interval is the mean attempt period  $\tau_{APm}$ .

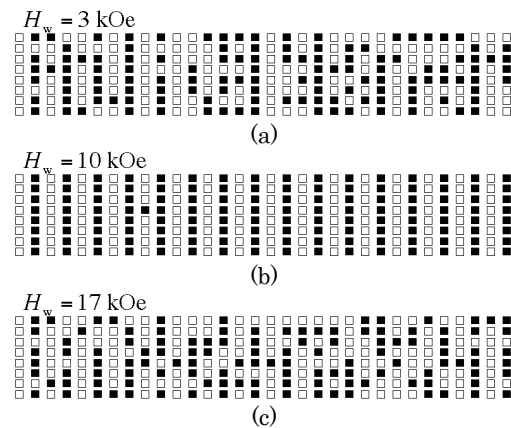
## 3. Calculation Results

### 3.1 1 column/bit and $\alpha = 0.1$

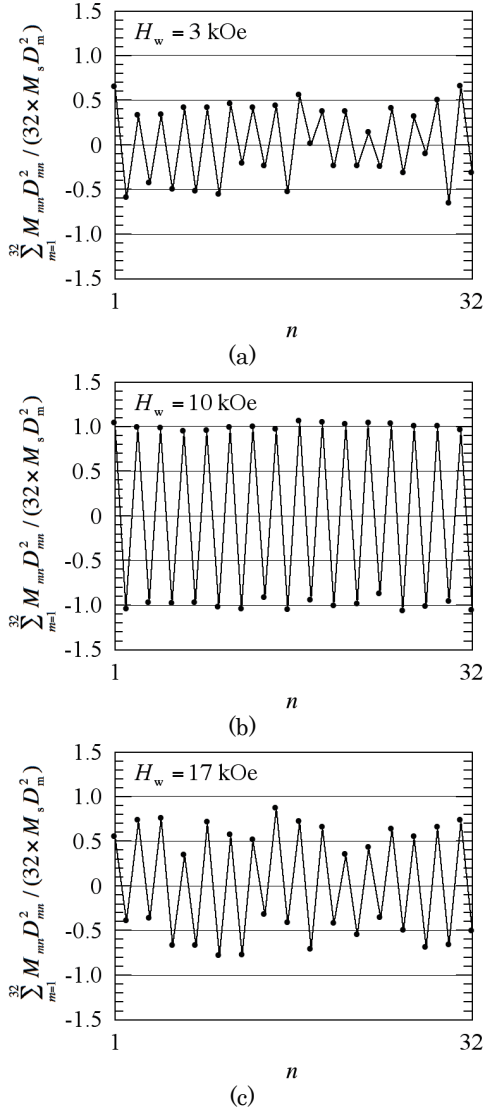
Representative grain magnetization patterns calculated employing our model are shown in Fig. 3 under the conditions of 1 column/bit, damping constant  $\alpha = 0.1$ , and typical values. A writing field  $H_w$  of about 10 kOe is the best condition (see Fig. 6 (a)),  $H_w = 3$  kOe is too small, and  $H_w = 17$  kOe is too large.

Figure 4 shows the summation of the surface magnetic charge  $M_{mn}D_{mn}^2$  for the cross-track direction  $m$  as a function of the position for the down-track direction  $n$  where  $M_{mn}$  and  $D_{mn}$  are the magnetization and the grain size for the grain arrangement matrix  $(m, n)$ , respectively, the vertical axis is normalized by  $32 \times M_s D_m^2$ , and  $M_{mn} = M_s$  since  $\sigma_{Tc}/T_c = 0$ . The surface charge summation is proportional to the signal amplitude read by the head with infinite resolution. The surface charge summations for Figs. 4 (a) and (c) are unsaturated according to the grain magnetization patterns for Figs. 3 (a) and (c), respectively.

This can be explained using the time dependence of the grain magnetization reversal probability  $P_{\pm}$  for various  $H_w$  values as shown in Fig. 5. Normal write-error (WE)<sup>2)</sup> means that the magnetization does not switch to the recording direction, and WE occurs during writing ( $0 \leq t < \tau_{min}$ ). The attempt number is important when  $P_{\pm}$  is high. For  $H_w = 3$  kOe, since the attempt number, that is, the filled circle number, is small when  $P_{\pm}$  is high, WE occurs. On the other hand, erasure-after-write (EAW)<sup>2)</sup> is the grain magnetization reversal in the opposite direction to the recording direction caused by changing the  $H_w$  direction at the end of the writing time  $\tau_{min}$ , and EAW occurs after writing ( $t \geq \tau_{min}$ ). The  $P_{\pm}$  value is important at the end of the writing time  $\tau_{min}$ . For  $H_w = 17$  kOe, since the  $P_{\pm}$  value at  $\tau_{min}$  designated by an open circle is not sufficiently low, EAW occurs. For  $H_w = 10$  kOe, the attempt number is sufficiently large when  $P_{\pm}$  is high,



**Fig. 3** Representative grain magnetization patterns for (a) writing field  $H_w = 3$  kOe, (b) 10 kOe, and (c) 17 kOe under conditions of 1 column/bit, damping constant  $\alpha = 0.1$ , and typical values.



**Fig. 4** Summation of surface magnetic charges  $M_{mm}D_{mm}^2$  for cross-track direction  $m$  as a function of position for down-track direction  $n$  under conditions of 1 column/bit,  $\alpha = 0.1$ , and typical values.

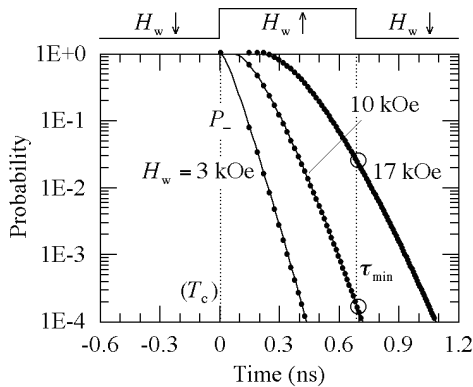


**Fig. 5** Time dependence of grain magnetization reversal probability  $P_-$  for various  $H_w$  values under conditions of 1 column/bit,  $\alpha = 0.1$ , and typical values.

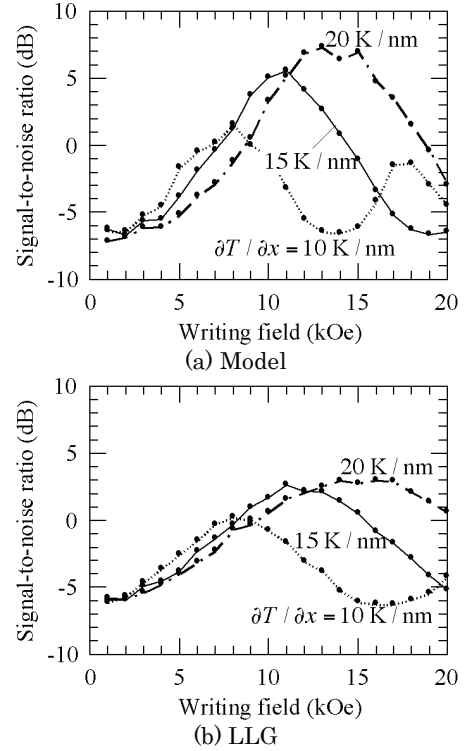


**Fig. 6** Dependence of signal-to-noise ratio on writing field. (a) Model calculation and (b) micromagnetic (LLG) calculation for various thermal gradients  $\partial T / \partial x$  under conditions of 1 column/bit,  $\alpha = 0.1$ , and linear velocity  $v = 10$  m/s.

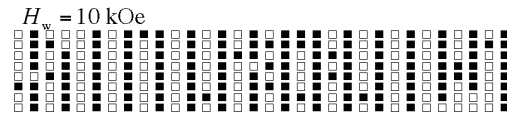


**Fig. 7** Representative grain magnetization patterns calculated employing a micromagnetic calculation for writing field  $H_w = 10$  kOe under conditions of 1 column/bit, damping constant  $\alpha = 0.1$ , and typical values.

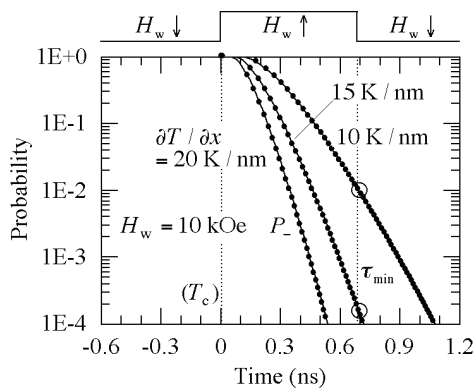
and the  $P_-$  value at  $\tau_{min}$  designated by an open circle is sufficiently low. Therefore, both WE and EAW are low.

Figure 6 (a) shows the dependence of the signal-to-noise ratio (SNR) on the writing field  $H_w$  for various thermal gradients  $\partial T / \partial x$  calculated employing our model. The increase in SNR as  $H_w$  increases in a low  $H_w$  region is caused by a reduction in WE since WE means that the magnetization does not switch to the recording direction during writing, and WE is caused by an insufficient  $H_w$ . The decrease in SNR as  $H_w$  increases in a high  $H_w$  region is caused by EAW since EAW is the magnetization reversal in the opposite direction to the recording direction after writing, and EAW is caused by an excessive  $H_w$ . The increase in SNR as  $H_w$  increases at more than about 14 kOe for  $\partial T / \partial x = 10$  K/nm in Fig. 6 (a) is caused by after-write (AW). AW occurs after writing ( $t \geq \tau_{min}$ ).

Therefore, if the written data is “101010” for “write”, it is “010101” for “after-write”.

The results in Fig. 6 (a) can be compared with those in Fig. 6 (b), which were determined employing a micromagnetic calculation using the LLG equation. Although AW for  $\partial T/\partial x = 10$  K/nm in Fig. 6 (b) is underestimated, the tendencies are almost the same.

The maximum SNR value in Fig. 6 (b) is lower than that in Fig. 6 (a). This is attributed to the difference between the grain magnetization patterns in Fig. 7 and in Fig. 3 (b). There are many error grains in the grain pattern calculated employing a micromagnetic calculation for  $H_w = 10$  kOe as shown in Fig. 7. The writing field at which the SNR value shows the maximum in Fig. 6 (b) is somewhat higher than that in Fig. 6 (a). This is attributed to the determination method of the attempt time in our model calculation described in 2.2. In this way, although our model calculation is a coarse estimation, the tendencies of the results in Figs. 6 (a) and (b) are almost the same.



**Fig. 8** Time dependence of grain magnetization reversal probability  $P_-$  for various  $\partial T/\partial x$  values under conditions of 1 column/bit,  $\alpha = 0.1$ , and  $v = 10$  m/s.

A large dependence of EAW on  $\partial T/\partial x$  can be seen in Fig. 6. Figure 8 shows the time dependence of grain reversal probability  $P_-$  for various thermal gradients  $\partial T/\partial x$  at  $H_w = 10$  kOe. The  $P_-$  values at  $\tau_{\min}$  designated by open circles are important for EAW, and  $P_-$  abruptly decreases as  $\partial T/\partial x$  increases as shown in Fig. 8. Therefore, increasing  $\partial T/\partial x$  is effective in decreasing EAW as shown in Fig. 6.

On the other hand, the attempt number is important for WE when  $P_-$  is high. The attempt numbers are about 11, 7, and 5 for  $\partial T/\partial x = 10, 15,$  and  $20$  K/nm, respectively, when  $0.1 \leq P_- \leq 1$  as shown in Fig. 8. Even if the attempt number for  $\partial T/\partial x = 20$  K/nm is five, it is enough to suppress WE. Therefore, the dependence of WE on  $\partial T/\partial x$  is small as shown in Fig. 6.

Next, Fig. 9 shows the dependence of SNR on  $H_w$  for various linear velocities  $v$ . A large dependence of WE and a small dependence of EAW on  $v$  can be seen. The  $\tau_{\min} = D_{BP}/v$  ( $D_{BP} = 6.8$  nm) values are 1.36, 0.68, and 0.34 ns for  $v = 5, 10,$  and  $20$  m/s, respectively, as

shown in Fig. 10. The attempt numbers are about 14, 7, and 3 for  $v = 5, 10,$  and  $20$  m/s, respectively, when  $0.1 \leq P_- \leq 1$  at  $H_w = 10$  kOe. Since the attempt number for  $v = 20$  m/s is not sufficiently large to suppress WE, reducing  $v$  is effective in decreasing WE. In other words, reducing  $v$  is effective in increasing the writing field sensitivity.

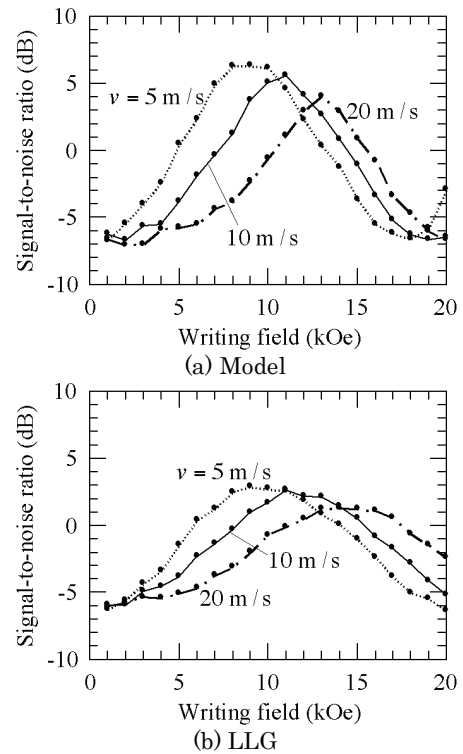


**Fig. 9** Dependence of signal-to-noise ratio on writing field. (a) Model calculation and (b) micromagnetic (LLG) calculation for various  $v$  values under conditions of 1 column/bit,  $\alpha = 0.1$ , and  $\partial T/\partial x = 15$  K/nm.

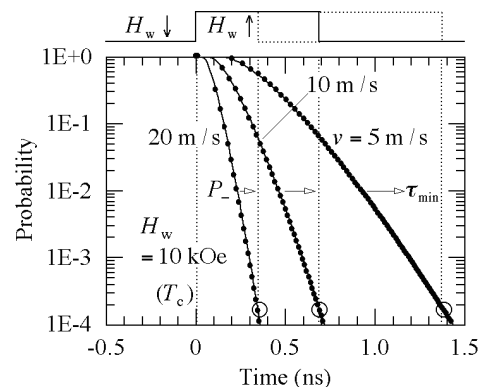


**Fig. 10** Time dependence of grain magnetization reversal probability  $P_-$  for various  $v$  values under conditions of 1 column/bit,  $\alpha = 0.1$ , and  $\partial T/\partial x = 15$  K/nm.

On the other hand, the temperatures at  $\tau_{\min}$  are the same regardless of the  $v$  values since the thermal gradient is constant. Then, the  $P_-$  values at  $\tau_{\min}$  are



the same regardless of the  $v$  values designated by open circles in Fig. 10. Therefore, the dependence of EAW on  $v$  is small.

In addition to the fact that the tendencies of the results in Figs. 6 (a) and (b) are almost the same, those in Figs. 9 (a) and (b) are also almost the same. Therefore, our model calculation can be used for HAMR design. The writing process can be described using the temperature dependences of the grain magnetization reversal probability and the attempt number in our model. A feature of our model calculation is that the interpretation of the result and the establishment of HAMR design policy are easy. Furthermore, since the calculation time of our model is short, we can calculate the bit error rate using  $10^5$  or  $10^6$  bits in a short time. Bit error rate data are useful for determining whether or not recording is possible, and our work on this topic will be published elsewhere<sup>12)</sup>.

**3.2 1 column/bit and  $\alpha = 0.01$**

We also discuss the writing property with the damping constant  $\alpha = 0.01$  instead of 0.1.

Figure 11 shows representative grain magnetization patterns calculated employing our model. When  $\alpha = 0.1$ , the surface charge summation saturated at  $H_w = 10$  kOe, as shown in Fig. 4 (b). However, when  $\alpha = 0.01$ , the surface charge summation increased slowly with  $H_w$  and was unsaturated even at  $H_w = 17$  kOe, as shown in Fig. 12. Therefore, WE was dominant and writing was very difficult when  $\alpha = 0.01$ .

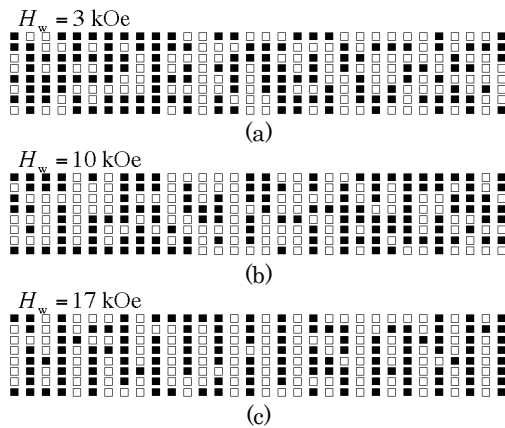


**Fig. 11** Representative grain magnetization patterns for (a)  $H_w = 3$  kOe, (b) 10 kOe, and (c) 17 kOe under conditions of 1 column/bit,  $\alpha = 0.01$ , and typical values.

The time dependence of  $P_-$  for various  $H_w$  values is shown in Fig. 13. Although the  $P_-$  values shown in Figs. 5 and 13 are identical, the attempt number decreases to about one tenth as shown in Fig. 13, and there is almost no opportunity for writing. Therefore, WE is dominant. Since the attempt number is small when  $P_-$  is high,  $P_-$  must be increased for writing.  $P_-$

can be increased by increasing  $H_w$  in consideration of Eqs. (1) and (3). Therefore, a higher  $H_w$  is necessary when  $\alpha = 0.01$ .

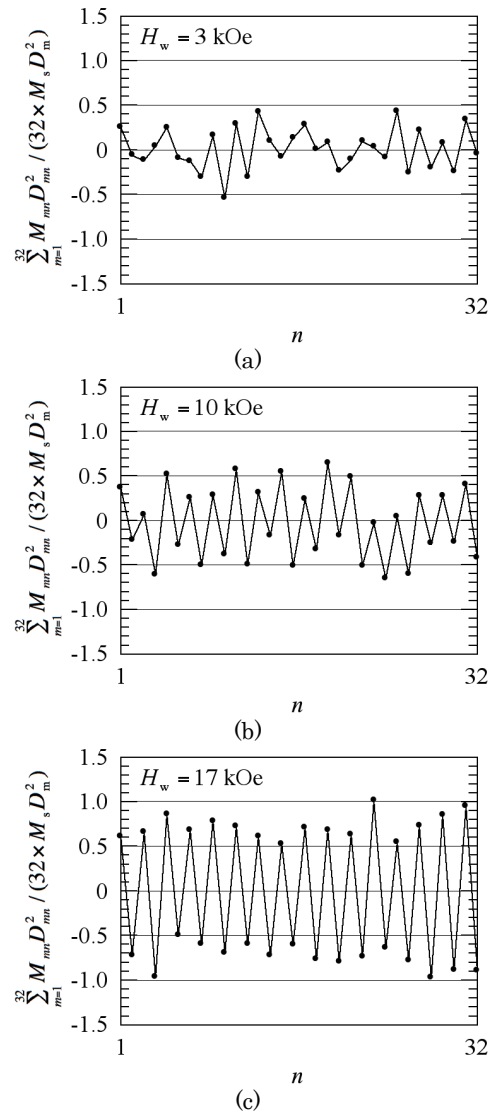


**Fig. 12** Summation of surface magnetic charges  $M_{mn}D_{mn}^2$  for cross-track direction  $m$  as a function of position for down-track direction  $n$  under conditions of 1 column/bit,  $\alpha = 0.01$ , and typical values.

The dependence of SNR on  $H_w$  for various thermal gradients  $\partial T / \partial x$  is shown in Fig. 14. No dependence of SNR on  $\partial T / \partial x$  can be seen for either (a) Model or (b) LLG calculations since WE is dominant and changing  $\partial T / \partial x$  is not effective in decreasing WE as mentioned in 3.1.

As also mentioned in 3.1, we expect reducing the linear velocity  $v$  to be effective in decreasing WE. Figure 15 shows the dependence of SNR on  $H_w$  for various  $v$  values regarding both (a) Model and (b) LLG calculations. As expected, when  $v$  is slow, writing becomes relatively easy since the attempt number increases from about 3 to 6 when  $0 \leq t \leq \tau_{\min}$  as  $v$  is reduced from 10 m/s to 5 m/s, as shown in Fig.

16. The decreasing SNR as  $H_w$  increases for a high  $H_w$  region in Fig. 15 is caused by EAW. EAW begins with a higher  $H_w$  than that when  $\alpha = 0.1$  in Fig. 9 since the attempt number for  $t \geq \tau_{\min}$  is also small for  $\alpha = 0.01$  as shown in Fig. 16. EAW in Fig. 15 (a) begins with a lower  $H_w$  than that in Fig. 15 (b). This is also attributed to the determination method of the attempt time as described in 3.1.

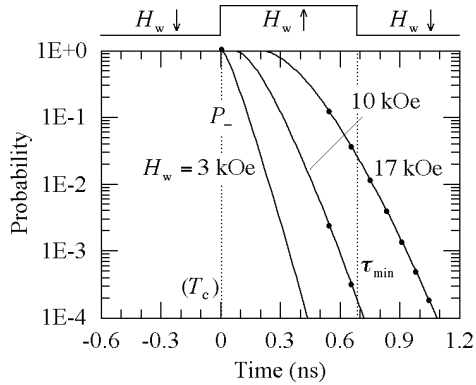


**Fig. 13** Time dependence of grain magnetization reversal probability  $P_-$  for various  $H_w$  values under conditions of 1 column/bit,  $\alpha = 0.01$ , and typical values.

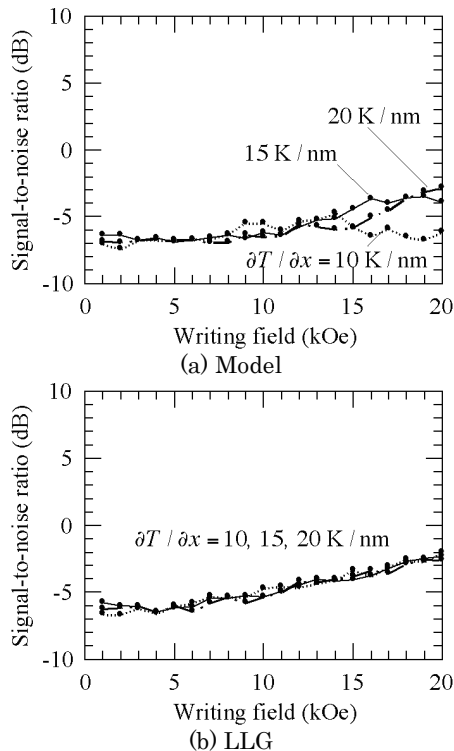


**Fig. 14** Dependence of signal-to-noise ratio on writing field. (a) Model calculation and (b) micromagnetic (LLG) calculation for various  $\partial T / \partial x$  values under conditions of 1 column/bit,  $\alpha = 0.01$ , and  $v = 10$  m/s.

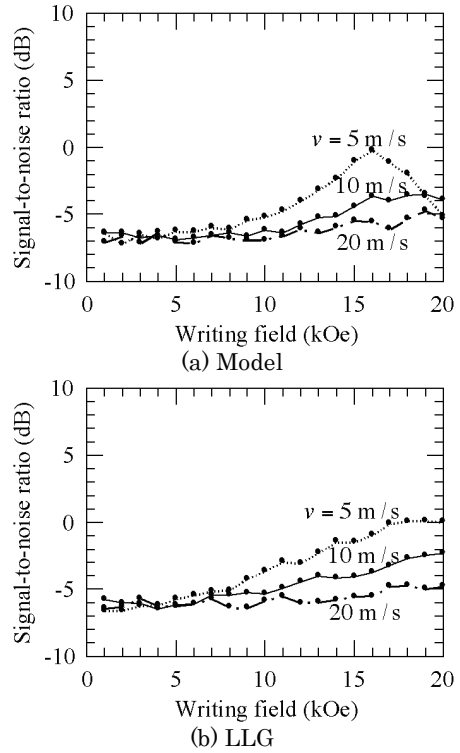


**Fig. 15** Dependence of signal-to-noise ratio on writing field. (a) Model calculation and (b) micromagnetic (LLG) calculation for various  $v$  values under conditions of 1 column/bit,  $\alpha = 0.01$ , and  $\partial T / \partial x = 15$  K/nm.

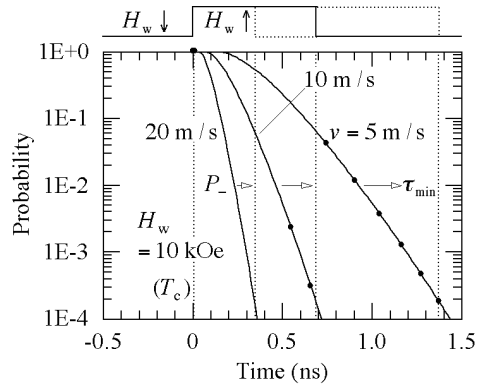


**Fig. 16** Time dependence of grain magnetization reversal probability  $P_-$  for various  $v$  values under conditions of  $\alpha = 0.01$ , and  $\partial T / \partial x = 15$  K/nm.

A serious problem in HAMR is that writing becomes difficult if the damping constant just below the Curie temperature is small. Whether or not writing is possible can be determined only by the bit error rate. Although the bit error rate data will be published elsewhere<sup>12)</sup>, the bit error rate for the medium with  $\alpha = 0.01$  is very high.

**3.3 4 columns/bit and  $\alpha = 0.1$**

Next, we discuss the writing property for 4 columns/bit instead of 1 column/bit.

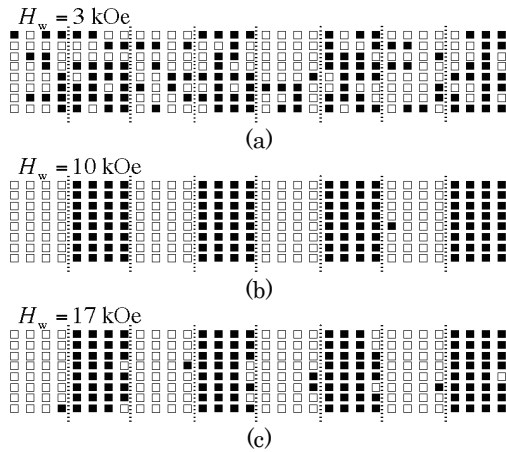


**Fig. 17** Representative grain magnetization patterns for (a)  $H_w = 3$  kOe, (b) 10 kOe, and (c) 17 kOe under conditions of 4 columns/bit,  $\alpha = 0.1$ , and typical values. Dotted lines indicate bit boundaries.

Representative grain magnetization patterns calculated employing our model are shown in Fig. 17. The dotted lines indicate bit boundaries. In Fig. 17 (a) the writing field  $H_w = 3$  kOe, write-error (WE) for 4 columns/bit is almost the same as that for 1 column/bit as shown in Fig. 3 (a). The  $H_w$  value of about 10 kOe is also the best condition for 4 columns/bit (see Fig. 20 (a)). However, when  $H_w = 17$  kOe, the degradation of the grain magnetization pattern caused by erasure-after-write (EAW) for 4 columns/bit as shown in Fig. 17 (c) is remarkably small compared with that for 1 column/bit as shown in Fig. 3 (c). EAW occurs only at the 4th column in one bit as shown in Fig. 17 (c). This is confirmed by the summation of the surface magnetic charge  $M_{mn}D_{mn}^2$  as shown in Figs. 4 and 18. The surface charge summation is unsaturated only at the 4th column in one bit as shown in Fig. 18 (c) according to the grain magnetization patterns for Fig. 17 (c). The same phenomenon can be seen in a previous paper<sup>13</sup>.

This can be explained using the time dependence of the grain magnetization reversal probability  $P_-$  for  $H_w = 17$  kOe as shown in Fig. 19. The times corresponding to the Curie temperatures  $T_{c1}$ ,  $T_{c2}$ ,  $T_{c3}$ , and  $T_{c4}$  are 0, 0.68, 1.37, and 2.05 ns for the 1st, 2nd, 3rd, and 4th column, respectively, and the end of the writing time  $\tau_{min}$  is 2.73 ns. Therefore, the writing time for the 1st column is 2.73 ns ( $= 2.73 - 0$  ns). Since the writing time is long,  $P_-$  for the 1st column at  $\tau_{min}$  is sufficiently low and EAW does not occur. Similarly, the writing times for the 2nd and 3rd column are 2.05 ( $= 2.73 - 0.68$ ) and 1.36 ns ( $= 2.73 - 1.37$  ns), respectively. EAW does not occur since the writing times are long. However, the writing time for the 4th column is only 0.68 ns ( $= 2.73 - 2.05$  ns), which is the same as in Fig. 5. Therefore, EAW occurs only at the 4th column in one bit since  $P_-$  at  $\tau_{min}$  designated by an open circle is insufficiently low only for the 4th column.

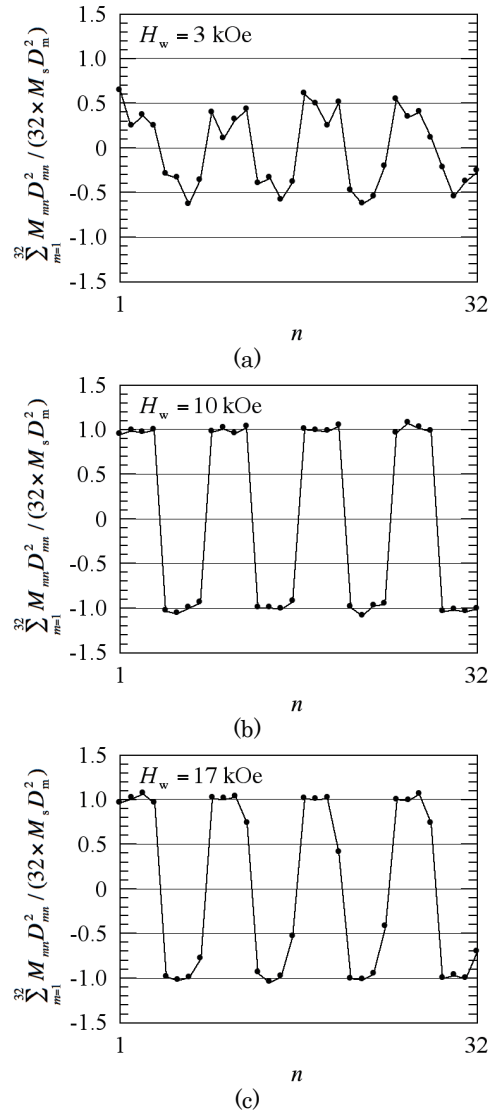


**Fig. 18** Summation of surface magnetic charges  $M_{mn}D_{mn}^2$  for cross-track direction  $m$  as a function of position for down-track direction  $n$  under conditions of 4 columns/bit,  $\alpha = 0.1$ , and typical values.

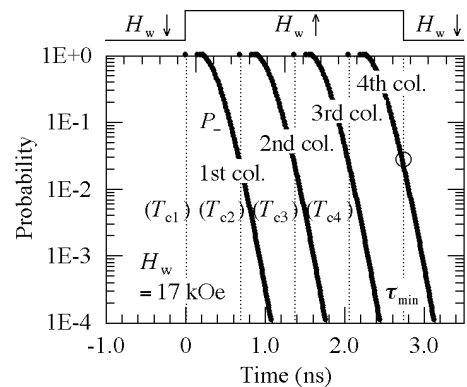


**Fig. 19** Time dependence of grain magnetization reversal probability  $P_-$  for  $H_w = 17$  kOe under conditions of 4 columns/bit,  $\alpha = 0.1$ , and typical values.

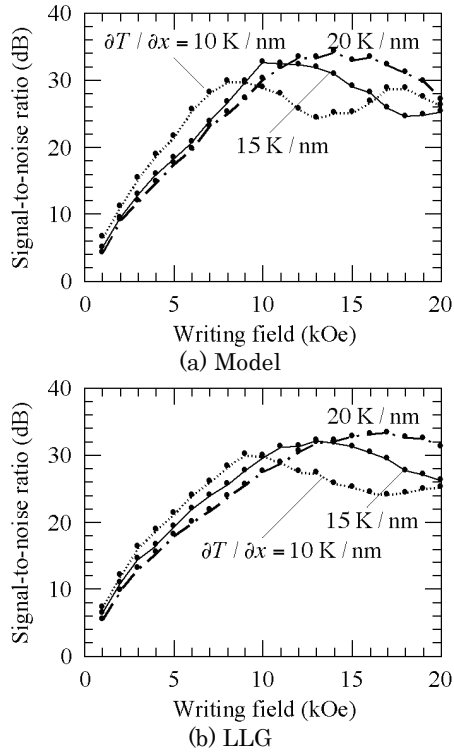


**Fig. 20** Dependence of signal-to-noise ratio on writing field. (a) Model calculation and (b) micromagnetic (LLG) calculation for various  $\partial T / \partial x$  values under conditions of 4 columns/bit,  $\alpha = 0.1$ , and  $v = 10$  m/s.

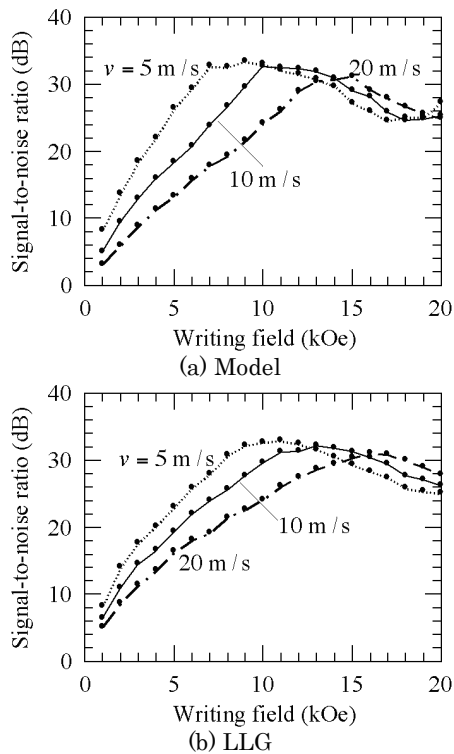


**Fig. 21** Dependence of signal-to-noise ratio on writing field. (a) Model calculation and (b) micromagnetic (LLG) calculation for various  $v$  values under conditions of 4 columns/bit,  $\alpha = 0.1$ , and  $\partial T / \partial x = 15$  K/nm.

Figure 20 shows the dependence of SNR on  $H_w$  for various thermal gradients  $\partial T / \partial x$ . Since increasing  $\partial T / \partial x$  is effective in decreasing EAW as mentioned in 3.1, this effect can be seen in Fig. 20. However, the SNR improvement for EAW realized by increasing  $\partial T / \partial x$  is small since EAW occurs only in the 4th column. EAW and AW in Fig. 20 (a) begin with a lower  $H_w$  than that in Fig. 20 (b). This is also attributed to the determination method of the attempt time as described in 3.1.

On the other hand, WE occurs in every column<sup>2)</sup>. Therefore, decreasing linear velocity  $v$  is effective in improving the SNR for WE as shown in Fig. 21. In other words, reducing  $v$  is effective in increasing the writing field sensitivity.

The SNR values necessary for a certain value of bit error rate (BER), for example  $10^{-3}$ , are approximately the same for 1 and 4 columns/bit. The SNR value for 4 columns/bit is higher than that for 1 column/bit. This implies that the writing field necessary for  $\text{BER} = 10^{-3}$  decreases and the writing field sensitivity increases as the column number increases. This issue is a statistics problem and will be discussed elsewhere<sup>12)</sup>.

### 3.4 4 columns/bit and $\alpha = 0.01$

Finally, we discuss the writing properties for 4 columns/bit and  $\alpha = 0.01$ .

Representative grain magnetization patterns calculated employing our model are shown in Fig. 22. Although EAW can be seen only in the 4th column in Fig. 17 (c) for  $\alpha = 0.1$  and  $H_w = 17$  kOe, error occurs in every column in Fig. 22 (c) for  $\alpha = 0.01$  and  $H_w = 17$  kOe. Furthermore, the surface charge summation increases as  $H_w$  increases as shown in Fig. 23. Therefore, WE is dominant even for  $H_w = 17$  kOe.

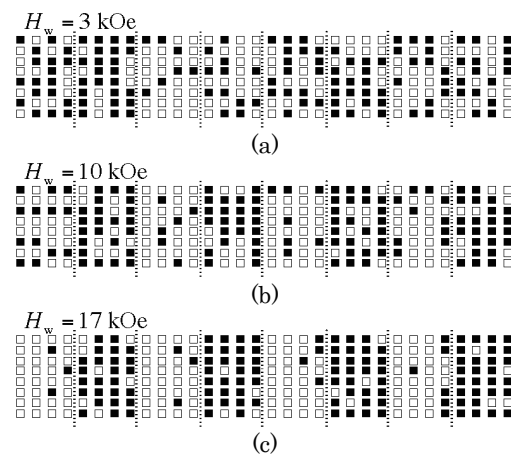


**Fig. 22** Representative grain magnetization patterns for (a)  $H_w = 3$  kOe, (b) 10 kOe, and (c) 17 kOe under conditions of 4 columns/bit,  $\alpha = 0.01$ , and typical values. Dotted lines indicate bit boundaries.



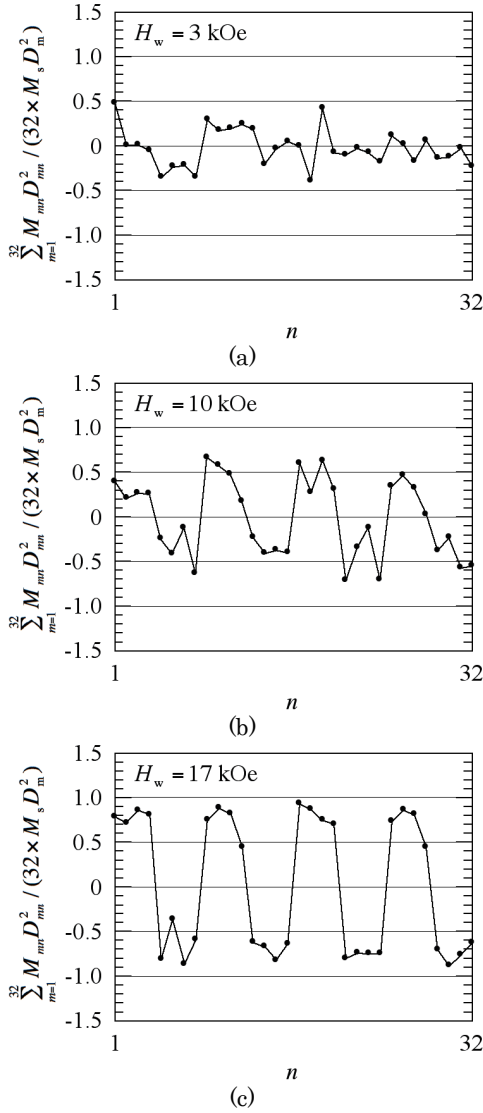


**Fig. 23** Summation of surface magnetic charges  $M_{mn}D_{mn}^2$  for cross-track direction  $m$  as a function of position for down-track direction  $n$  under conditions of 4 columns/bit,  $\alpha = 0.01$ , and typical values.

The dependence of SNR on  $H_w$  for various thermal gradients  $\partial T / \partial x$  is shown in Fig. 24, and for various linear velocities  $v$  in Fig. 25. Since WE is dominant, no SNR improvement in  $\partial T / \partial x$  or improvement in  $v$  can be seen in Figs. 24 and 25, respectively.

The SNR value for 4 columns/bit and  $\alpha = 0.01$  is higher than that for 1 column/bit and  $\alpha = 0.01$ . Therefore, writing becomes possible for 4 columns/bit even if  $\alpha = 0.01$ . This issue is also a statistics problem and will be discussed elsewhere<sup>12)</sup>.

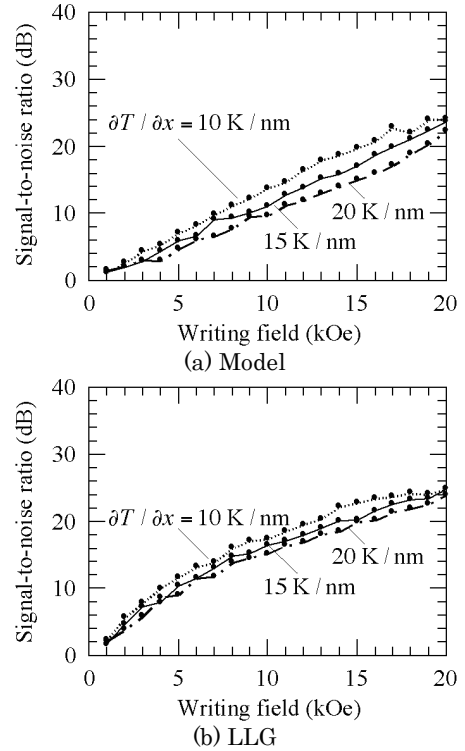


**Fig. 24** Dependence of signal-to-noise ratio on writing field. (a) Model calculation and (b) micromagnetic (LLG) calculation for various  $\partial T / \partial x$  values under conditions of 4 columns/bit,  $\alpha = 0.01$ , and  $v = 10$  m/s.

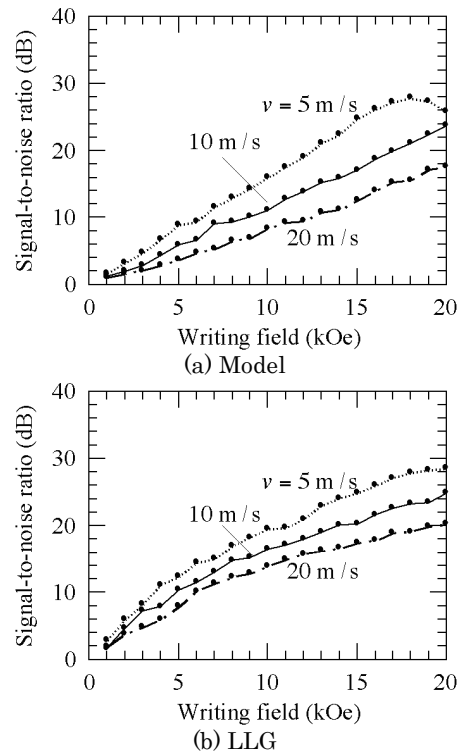


**Fig. 25** Dependence of signal-to-noise ratio on writing field. (a) Model calculation and (b) micromagnetic (LLG) calculation for various  $v$  values under conditions of 4 columns/bit,  $\alpha = 0.01$ , and  $\partial T / \partial x = 15$  K/nm.

#### 4. Conclusions

We calculated the dependence of the signal-to-noise ratio on the writing field for heat-assisted magnetic recording (HAMR) for various calculation parameters by employing both our improved model calculation and the conventionally used micromagnetic calculation. The tendencies of the results in the model calculation and the micromagnetic calculation were almost the same. Therefore, our model calculation can be used for HAMR design. The writing process can be described using the temperature dependences of the grain magnetization reversal probability and the attempt number.

If the Gilbert damping constant is small, writing is difficult and a higher writing field is necessary since the attempt number is small.

Write-errors can be reduced by reducing the linear velocity since the attempt number increases when the grain magnetization reversal probability is high.

Erase-after-write can be reduced by increasing the thermal gradient and/or the grain column number since the grain magnetization reversal probability becomes low at the end of the writing time.

**Acknowledgement** We acknowledge the support of the Advanced Storage Research Consortium (ASRC), Japan.

#### References

- 1) S. H. Charap, P. -L. Lu, and Y. He: *IEEE Trans. Magn.*, **33**, 978 (1997).
- 2) T. Kobayashi, F. Inukai, K. Enomoto, and Y. Fujiwara: *J. Magn. Soc. Jpn.*, **41**, 1 (2017).
- 3) T. Kobayashi, Y. Nakatani, F. Inukai, K. Enomoto, and Y. Fujiwara: *J. Magn. Soc. Jpn.*, **41**, 52 (2017).
- 4) T. Kobayashi, Y. Nakatani, K. Enomoto, and Y. Fujiwara: *J. Magn. Soc. Jpn.*, **42**, 15 (2018).
- 5) T. Kobayashi, Y. Isowaki, and Y. Fujiwara: *J. Magn. Soc. Jpn.*, **40**, 28 (2016).
- 6) T. Kobayashi, Y. Isowaki, and Y. Fujiwara: *J. Magn. Soc. Jpn.*, **39**, 8 (2015).
- 7) M. Mansuripur, and M. F. Ruane: *IEEE Trans. Magn.*, **MAG-22**, 33 (1986).
- 8) J. -U. Thiele, K. R. Coffey, M. F. Toney, J. A. Hedstrom, and A. J. Kellock: *J. Appl. Phys.*, **91**, 6595 (2002).
- 9) Y. Nakatani, Y. Uesaka, N. Hayashi, and H. Fukushima: *J. Magn. Magn. Mat.*, **168**, 347 (1997).
- 10) E. D. Boerner and H. N. Bertram: *IEEE Trans. Magn.*, **34**, 1678 (1998).
- 11) Y. Kanai, Y. Jinbo, T. Tsukamoto, S. J. Greaves, K. Yoshida, and H. Muraoka: *IEEE Trans. Magn.*, **46**, 715 (2010).
- 12) T. Kobayashi, Y. Nakatani, and Y. Fujiwara: *J. Magn. Soc. Jpn.*, **42**, 110 (2018).
- 13) J. -G. Zhu and H. Li: *IEEE Trans. Magn.*, **49**, 765 (2013).

**Received Apr. 11, 2018; Accepted Aug. 31, 2018**

## Editorial Committee Members · Paper Committee Members

K. Kobayashi and T. Ono (Director), T. Kato, K. Koike and T. Taniyama (Secretary)					
A. Fujita	H. Goto	H. Hashino	S. Honda	S. Inui	Y. Kanai
S. Kasai	A. Kikitsu	H. Kikuchi	T. Kimura	T. Kubota	K. Miura
T. Nagahama	H. Naganuma	M. Naoe	M. Ohtake	N. Pham	T. Sasayama
T. Sato	T. Sato	K. Sekiguchi	M. Sekino	T. Shima	Y. Shiratsuchi
M. Sonehara	T. Tanaka	S. Yamada	K. Yamamoto	H. Yuasa	
N. Adachi	K. Bessho	M. Doi	T. Doi	T. Hasegawa	N. Inaba
S. Isogami	K. Kamata	H. Kato	K. Kato	T. Koda	S. Kokado
Y. Kota	T. Maki	E. Miyashita	T. Morita	S. Muroga	H. Nakayama
T. Narita	D. Oyama	J. Ozeki	T. Saito	S. Seino	K. Tajima
M. Takezawa	T. Takura	M. Tsunoda	S. Yabukami	T. Yamamoto	K. Yamazaki
S. Yoshimura					

### Notice for Photocopying

If you wish to photocopy any work of this publication, you have to get permission from the following organization to which licensing of copyright clearance is delegated by the copyright owner.

〈All users except those in USA〉

Japan Academic Association for Copyright Clearance, Inc. (JAACC)  
6-41 Akasaka 9-chome, Minato-ku, Tokyo 107-0052 Japan  
Phone 81-3-3475-5618 FAX 81-3-3475-5619 E-mail: info@jaacc.jp

〈Users in USA〉

Copyright Clearance Center, Inc.  
222 Rosewood Drive, Danvers, MA01923 USA  
Phone 1-978-750-8400 FAX 1-978-646-8600

### 編集委員・論文委員

小林宏一郎 (理事)	小野輝男 (理事)	加藤剛志 (幹事)	小池邦博 (幹事)	谷山智康 (幹事)					
乾成里	大竹充	葛西伸哉	金井靖	喜々津哲	菊池弘昭	木村崇	窪田崇秀	後藤博樹	
笹山瑛由	佐藤拓	佐藤岳	嶋敏之	白土優	関口康爾	関野正樹	曾根原誠	田中哲郎	
直江正幸	永沼博	長浜太郎	橋野早人	PHAM NAMHAI		藤田麻哉	本多周太	三浦健司	
山田晋也	山本健一	湯浅裕美							
安達信泰	磯上慎二	稲葉信幸	小瀬木淳一	小山大介	加藤宏朗	加藤和夫	鎌田清孝	神田哲典	
古門聡士	小田洋平	齊藤敏明	清野智史	田倉哲也	竹澤昌晃	田島克文	角田匡清	土井達也	
土井正晶	中山英俊	成田正敬	長谷川崇	別所和宏	榎智仁	宮下英一	室賀翔	森田孝	
藪上信	山崎慶太	山本崇史	吉村哲						

### 複写をされる方へ

本会は下記協会に複写に関する権利委託をしていますので、本誌に掲載された著作物を複写したい方は、同協会より許諾を受けて複写して下さい。但し(社)日本複写権センター(同協会より権利を再委託)と包括複写許諾契約を締結されている企業の社員による社内利用目的の複写はその必要はありません。(社外頒布用の複写は許諾が必要です。)

権利委託先：一般社団法人学術著作権協会

〒107-0052 東京都港区赤坂9-6-41 乃木坂ビル

電話 (03) 3475-5618 FAX (03) 3475-5619 E-mail: info@jaacc.jp

なお、著作者の転載・翻訳のような、複写以外の許諾は、学術著作権協会では扱っていませんので、直接本会へご連絡ください。

本誌掲載記事の無断転載を禁じます。

## Journal of the Magnetism Society of Japan

Vol. 42 No. 6 (通巻第 300 号) 2018 年 11 月 1 日発行

Vol. 42 No. 6 Published Nov. 1, 2018

by the Magnetism Society of Japan

Tokyo YWCA building Rm207, 1-8-11 Kanda surugadai, Chiyoda-ku, Tokyo 101-0062

Tel. +81-3-5281-0106 Fax. +81-3-5281-0107

Printed by JP Corporation Co., Ltd.

2-3-36, Minamikase, Saiwai-ku, Kanagawa 212-0055

Advertising agency: Kagaku Gijutsu-sha

発行：(公社)日本磁気学会 101-0062 東京都千代田区神田駿河台 1-8-11 東京YWCA会館 207 号室

製作：ジェイビーコーポレーション 212-0055 神奈川県川崎市幸区南加瀬 2-3-36 Tel. (044) 571-5815

広告取扱い：科学技術社 111-0052 東京都台東区柳橋 2-10-8 武田ビル 4F Tel. (03) 5809-1132

Copyright © 2018 by the Magnetism Society of Japan